PRODUCTION OF DRELL–YAN PAIRS IN pp COLLISIONS

S. GAVIN[a], S. GUPTA[b], R. KAUFFMAN[a], P. V. RUUSKANEN[c], D. K. SRIVASTAVA[d] and R. L. THEWS[e]

[a] *Department of Physics, Brookhaven National Laboratory, Upton, New York 11973, USA*
[b] *Theory Group, Tata Institute of Fundamental Research, Homi Bhabha Road, Bombay 400 005, India*
[c] *Institute for Theoretical Physics, P.O.Box 9, FIN-00014, University of Helsinki, Finland*
[d] *Variable Energy Cyclotron Centre, 1/AF Bidhan Nagar, Calcutta 700 064, India*
[e] *Department of Physics, University of Arizona, Tucson, Arizona 85721, USA*

We compute cross sections for the Drell-Yan process in N–N collisions at next-to-leading order in α_s. The mass, rapidity, transverse momentum, and angular dependence of these cross sections are presented. An estimate of higher order corrections is obtained from next-to-next-to-leading order calculation of the mass distribution. We compare the results with some of the existing data to show the quality of the agreement between calculations and data. We present predictions for energies which will become available at the RHIC and LHC colliders. Uncertainties in these predictions due to choices of scale, scheme and parton distribution are discussed.

INTRODUCTION

The aim of this study is to provide a systematic survey of theoretical predictions for the Drell–Yan process [1, 2] in nucleon–nucleon collisions at energies relevant to ion–ion experiments at RHIC and LHC, and to discuss confidence limits for these predictions. In an accompanying article, Van Neerven has reviewed the theory of the Drell–Yan process, emphasizing the dependence of the production rate on the dilepton's mass M and rapidity y. We present calculations of the M and y distributions using standard perturbative QCD. To supplement these calculations, we provide a skeletal theoretical discussion to fix the notation and identify the uncertainties. In addition, we study the experimentally-relevant transverse momentum and angular distributions of the dileptons. These topics are treated in separate subsections, since one must go beyond perturbation theory to compute these distributions.

Our predictions for $\mathrm{d}\sigma/\mathrm{d}M\mathrm{d}y$ are based on a perturbative analysis of the underlying partonic processes to order α_s [3, 4, 5, 6]. Results for $\mathrm{d}\sigma/\mathrm{d}M$ are reported to order α_s^2. We find that the perturbative corrections grow as M decreases. From the point of view of the heavy ion physics, the mass region from 3 to 10 GeV is of most interest. The relative magnitude of the $O(\alpha_s^2)$ correction in this range sets one limit on our confidence in the applicability of perturbation theory.

At fixed order the calculated cross sections depend on the renormalization scale μ_R, the factorization scale μ_F, and the regularization scheme. The form of the renormalized hard-scattering matrix elements and the definition of the parton distributions are specified by the regularization scheme; DIS and $\overline{\rm MS}$ schemes are widely used. The physical quantities such as α_s that enter the matrix elements are defined at the scale μ_R, while the parton distributions are set at μ_F. Although these scales are related to the momentum transfer Q, the precise relation is process dependent and not unique. The standard parton distribution sets have been obtained assuming $\mu_F = \mu_R \equiv \mu$ [7, 8, 9].

The scale and scheme dependence of our calculations provides an additional measure of the accuracy of the perturbative description at the given order. From the standpoint of perturbation theory, the choices of scales and scheme are arbitrary — varying these choices introduces corrections at the next order in α_s. However, changing the scales and scheme in practice alters the numerical predictions for collisions in the kinematic range relevant to heavy ion experiments. In this work we discuss results for the DIS and $\overline{\rm MS}$ schemes and vary μ to test the scale dependence.

Confidence in our predictions at the LHC heavy ion energy $\sqrt{s} \sim 5.5$ A·TeV is further limited by current experimental uncertainties in the parton distributions. Specifically, the production of dileptons with $M < 10$ GeV in nucleon–nucleon collisions at this energy probes the parton distributions at Bjorken $x < 10^{-2}$. This region is accessible only to the ongoing experiments at HERA [10]. Consequently the differences between the various parton distribution sets is largest in this region [7, 8, 9]. We base our predictions on computations using state–of–the–art parton distribution sets that are consistent with the current (1994) HERA data. To illustrate the maximum uncertainty in these predictions, we compare these results to calculations using a recent set that does not exhibit the 'low-x rise' seen by HERA [10], MRS D0′. As the experiments accumulate data, these uncertainties will be reduced, thereby enabling more refined predictions before the start of the LHC program.

We outline the theory used to study the mass, rapidity, transverse momentum and angular distribution of the dileptons in the next section. In the following section we compare our results to data and obtain predictions for RHIC and LHC. Results for $d\sigma/dM dy$ are obtained using a code provided by W. van Neerven and P. Rijken. Transverse momentum spectra and angular distributions are obtained following Refs. [11] and [12] respectively. The computation of these distributions — and the p_T spectrum in particular — requires a partial resummation of the perturbation series together with nonperturbative input not contained in standard parton distributions. The methods and uncertainties specific to these processes are discussed in the appropriate subsections.

THEORETICAL BACKGROUND

We now discuss the calculation of the Drell–Yan cross section in perturbative QCD. Our goal here is to outline the theory so that the reader can make use of our numerical results without extensive recourse to the literature. We provide a list of essential references, but those who are interested in a more detailed discussion of should consult the accompanying article of van Neerven [2].

Mass Distributions

The lowest order contribution to the Drell Yan process is quark–antiquark annihilation into a lepton pair. The annihilation cross section can be obtained from the $e^+e^- \to \mu^+\mu^-$ cross section by including the color factor $1/3$ and the charge factor e_q^2 for the quarks. Since the variation of the center–of–mass energy $\sqrt{\hat{s}}$ of the incoming quark and antiquark leads to pairs of different masses, it is useful to consider a cross section that is differential in the mass M of the pair:

$$\frac{\mathrm{d}\hat{\sigma}}{\mathrm{d}M^2} = e_q^2 \hat{\sigma}_0 \delta(\hat{s} - M^2), \qquad \hat{\sigma}_0 = \frac{4\pi\alpha^2}{9M^2} \tag{1}$$

The four–momenta of the incoming partons are expressed in terms of the momentum fractions of the colliding hadrons as

$$p_1 = \frac{\sqrt{s}}{2}(x_1, 0, 0, x_1) \qquad\qquad p_2 = \frac{\sqrt{s}}{2}(x_2, 0, 0, -x_2), \tag{2}$$

where $\sqrt{s}$ is the center–of–mass energy of the hadrons. It follows that $\hat{s} = x_1 x_2 s$.

The lowest order hadronic cross section is now obtained by folding in the initial state quark and antiquark luminosities determined by the parton distribution functions:

$$\frac{\mathrm{d}\sigma}{\mathrm{d}M^2} = \hat{\sigma}_0 \int_0^1 dx_1 dx_2 \delta(x_1 x_2 s - M^2) \sum_k e_k^2 [q_k(x_1, \mu)\bar{q}_k(x_2, \mu) + (1 \leftrightarrow 2)]. \tag{3}$$

More precisely, the distributions q and $\bar{q}$ give the number densities of quarks and antiquarks at momentum fraction x and factorization scale μ which is of the order of M, the only scale entering the calculation of the mass distribution.

The momentum fractions of the incoming partons which contribute to the LO cross section can be expressed in terms of the rapidity of the pair, y, and a scaling variable $\tau = M^2/s$ as

$$x_{01} = \sqrt{\tau} e^y, \qquad x_{02} = \sqrt{\tau} e^{-y}. \tag{4}$$

Using $y = (1/2)\ln(x_{01}/x_{02})$, we write the double-differential cross section

$$\left(M^2 \frac{\mathrm{d}\sigma}{\mathrm{d}y\mathrm{d}M^2}\right)_{\mathrm{Born}} = \hat{\sigma}_0 \tau \sum_k e_k^2 [q_k(x_{01}, \mu)\bar{q}_k(x_{02}, \mu) + (1 \leftrightarrow 2)] = F(\tau, \mu), \tag{5}$$

exhibiting a scaling behavior in τ at leading order (apart from the logarithmic dependence on the factorization scale μ).

The inclusive lepton pair cross section also includes contributions from processes in which the final state contains partons in addition to the lepton pair. These processes are higher order in the QCD coupling $\alpha_{\rm s}$. Perturbative QCD provides a systematic way to calculate order by order in $\alpha_{\rm s}$, the contributions from such processes as well as from those with virtual quanta. Graphs for the next to leading order processes include Compton, annihilation, and vertex corrections. The complete next to leading order cross section is [3]

$$\begin{aligned}\left(\frac{{\rm d}\sigma}{{\rm d}y{\rm d}M^2}\right)_{\rm NLO} &= \frac{\hat{\sigma}_0}{s}\int_0^1 dx_1\, dx_2\, dz\, \delta(x_1x_2z-\tau)\delta(y-\frac{1}{2}\ln\frac{x_1}{x_2}) \\ &\times \left\{\left[\sum_k e_k^2(q_k(x_1)\bar{q}_k(x_2)+[1\leftrightarrow 2])\right]\left[\delta(1-z)+\frac{\alpha_{\rm s}(\mu)}{2\pi}f_q(z)\right]\right. \\ &+ \left.\left[\sum_k e_k^2(g(x_1)(q_k(x_2)+\bar{q}_k(x_2))+[1\leftrightarrow 2])\right]\left[\frac{\alpha_{\rm s}(\mu)}{2\pi}f_g(z)\right]\right\},\end{aligned} \tag{6}$$

where the g and q_k are evaluated at the scale μ. The correction terms in the DIS regularization scheme are

$$\begin{aligned}f_q(z) &= C_F\left[\delta(1-z)\left(1+\frac{4\pi^2}{3}\right)-6-4z+\left(\frac{3}{1-z}\right)_+ +2(1+z^2)\left(\frac{\ln(1-z)}{1-z}\right)_+\right], \\ f_g(z) &= \frac{1}{2}\left[(z^2+(1-z)^2\ln(1-z)+\frac{3}{2}-5z+\frac{9}{2}z^2\right].\end{aligned} \tag{7}$$

Similar terms can be written down for the $\overline{MS}$ scheme [6].

We will focus on the behavior of the cross section at next to leading order. Although a complete $\mathcal{O}(\alpha_{\rm s}^2)$ analysis exists for the total cross section and the rapidity integrated mass spectrum, the more experimentally useful double-differential cross section is known only to $\mathcal{O}(\alpha_{\rm s})$. The contributions from soft and virtual gluons, dominant at fixed target energies and $\tau >\ 0.01$ [2, 6], account for only part of the $\mathcal{O}(\alpha_{\rm s}^2)$ corrections to ${\rm d}\sigma/{\rm d}y{\rm d}M^2$ at the higher collider energies. On the other hand, we find below that the $\mathcal{O}(\alpha_{\rm s}^2)$ corrections to the rapidity integrated cross section are typically quite small for the kinematic range of interest. This result supports the reliability of the $\mathcal{O}(\alpha_{\rm s})$ prediction from (6) throughout the rapidity range that contributes most of the cross section. Such support is particularly useful in the low mass region ($M \sim M_{J/\psi}$), where a fast convergence of the perturbative series is far from self evident.

Transverse Momentum Distributions

Experiments show that the net transverse momenta of lepton pairs produced by the Drell-Yan process are of the order of 1 GeV for a dimuon mass, M, of 10 GeV. Such values are substantially smaller than the transverse momenta $\sim M/2$ carried by each of the leptons individually. On the other hand, the p_T of a Drell-Yan pair is much larger than the few-hundred MeV typical of soft QCD. If we neglect the transverse momentum of the incoming partons, then the lowest order process $q\bar{q} \to \gamma^* \to l^+l^-$ produces a final state with net $p_T = 0$. While any spread in the initial momentum will increase the final p_T on average, the intrinsic width of the parton distribution is rather small, $\langle p_T^2 \rangle_{\rm soft} \sim (0.3~{\rm GeV})^2$. This scale is determined by the inverse hadron size, since the target and projectile partons must be localized inside their parent hadrons. Therefore, we can attribute part of the measured p_T to the parton's intrinsic p_T, but not all.

The lepton pair acquires additional transverse momentum from production mechanisms that occur beyond leading order in perturbation theory [13, 14]. For example, in the Compton and annihilation processes

$$qg \to q\gamma^* \quad \text{and} \quad \bar{q}q \to \gamma^* g \tag{8}$$

p_T of the lepton pair can be balanced by the recoil of the final state quark or gluon. One can compute the p_T distribution perturbatively from these processes and their radiative corrections. The perturbation expansion is well behaved for $p_T \sim M$. However, at low p_T the expansion breaks down and a resummation of the perturbation series is required.

To see why this resummation is necessary, observe that the cross section in the region $p_T^2 \ll M^2$ is dominated by the leading-logarithm contributions:

$$\frac{{\rm d}\sigma}{{\rm d}p_T^2} \sim \frac{\alpha_{\rm s}}{p_T^2} \ln\left(\frac{M^2}{p_T^2}\right) \left[v_1 + v_2 \alpha_{\rm s} \ln^2\left(\frac{M^2}{p_T^2}\right) + v_3 \alpha_{\rm s}^2 \ln^4\left(\frac{M^2}{p_T^2}\right) + \cdots \right], \tag{9}$$

where $\alpha_{\rm s}$ is evaluated at the scale M^2. This series is effectively an expansion in $\alpha_{\rm s} \ln^2(M^2/p_T^2)$, rather than $\alpha_{\rm s}$ alone. The effective expansion parameter can be large at low p_T even if $\alpha_{\rm s}(M^2)$ is small. The leading-logarithm series (9) describes the effect of soft gluon radiation from the initial state q and $\bar{q}$ prior to their annihilation. Specifically, these logarithms are remnants of the mass and collinear singularities arising from the radiated gluons. The annihilation process in (8) contributes the term $\propto \alpha_{\rm s} \ln(M^2/p_T^2)/p_T^2$ and, in general, $q\bar{q} \to \gamma^* + n$ gluons produces the term of order $\alpha_{\rm s}^n$. Fortunately, the coefficients v_i of Eq. (9) are not independent and it is possible to sum the series exactly so that it applies even when $\alpha_{\rm s} \ln^2(M^2/p_T^2)$ is large [15, 16, 17, 18]. In addition, 'subleading' logarithm contributions, though smaller, can also be important.

The formalism needed to sum the leading and subleading logarithms was developed by Collins, Soper and Sterman [17]. For each species of colliding partons, one finds

$$M^2 \frac{{\rm d}\sigma}{{\rm d}p_T^2\, {\rm d}y {\rm d}M^2}({\rm resum}) = \pi \hat{\sigma}_0 \tau e_q^2 \int \frac{{\rm d}^2 b}{(2\pi)^2} e^{i\mathbf{b}\cdot\mathbf{p}_T} W(b), \tag{10}$$

$$\begin{aligned} W(b) \;&=\; \exp\left\{ -\int_{\beta^2/b^2}^{M^2} \frac{{\rm d}q^2}{q^2} \left[\ln\left(\frac{M^2}{q^2}\right) A\big(\alpha_{\rm s}(q^2)\big) + B\big(\alpha_{\rm s}(q^2)\big) \right] \right\} \\ &\quad \times (C \circ f_1)(x_1; \beta^2/b^2) \;\times\; (C \circ f_2)(x_2; \beta^2/b^2). \end{aligned} \tag{11}$$

where s is the total hadronic center-of-mass energy, f_1 and f_2 are the projectile and target parton distributions of the two colliding particles, and x_1 and x_2 defined by (4) are the dominant values of x as $p_T \to 0$. Note that the f_i can be q, $\overline{q}$ or g, depending on the process considered. The integration variable b is the impact parameter, the variable conjugate to p_T, and $\beta \equiv 2\ \mathrm{e}^{-\gamma_{\mathrm{E}}}$, where γ_{E} is Euler's constant. To obtain the total Drell–Yan rate at next-to-leading order, one must sum (10,11) over $q\bar{q}$, $g\bar{q}$ and gq initial states for all appropriate quark flavors; see Appendix A in ref. [11] for details. The function C is a coefficient function that converts the parton distributions f into distributions $C \circ f$ specific to the process at hand. The functions A, B, and $C(x)$ have perturbative expansions in α_{s}, with A and B starting at order α_{s}. The expansion for C begins at order 1 for quarks and order α_{s} for gluons. These functions can be extracted to a given order from the perturbative result, and have been determined for the Drell–Yan process at next-to-leading order by Davies *et al.* [19].

The resummed result (10,11) applies only when $p_T^2 \ll M^2$ because it includes only those terms that diverge as p_T^{-2} as $p_T \to 0$. Omitted in (10) are nonsingular contributions that are $\propto \{p_T^2 + M^2\}^{-1}$ at small p_T. At $p_T \sim M$ the singular and nonsingular contributions become comparable. On the other hand, conventional perturbation theory works well at large p_T, describing the complete p_T dependence to a given order in α_{s}.

Bridging the low–p_T and perturbative regimes is accomplished by adding in the terms that are not resummed, the so-called remainder or nonsingular terms. Arnold and Kauffman developed a prescription for calculating the remainder terms that explicitly matches the high and low p_T results. Their prescription proceeds as follows. One first expands the resummed result (10) in powers of α_{s}. This series, $\mathrm{d}\sigma/\mathrm{d}p_T^2\,\mathrm{d}y\mathrm{d}M^2(\mathrm{asym})$, contains the singular $1/p_T^2$ part of complete perturbation series $\mathrm{d}\sigma/\mathrm{d}p_T^2\,\mathrm{d}y\mathrm{d}M^2(\mathrm{pert})$. We refer to $\mathrm{d}\sigma/\mathrm{d}p_T^2\,\mathrm{d}y\mathrm{d}M^2(\mathrm{asym})$ as 'asymptotic' because it describes the perturbation series asymptotically as $p_T \to 0$. The asymptotic result in ref. [11] is expressed as convolutions of parton distributions with the coefficient functions of (11) and with Altarelli–Parisi splitting functions arising from the scale dependence of the parton distributions. With the singular terms isolated in the asymptotic result, the remainder is the difference between the perturbative result and the asymptotic result,

$$R = \frac{\mathrm{d}\sigma}{\mathrm{d}p_T^2\,\mathrm{d}y\mathrm{d}M^2}(\mathrm{pert}) - \frac{\mathrm{d}\sigma}{\mathrm{d}p_T^2\,\mathrm{d}y\mathrm{d}M^2}(\mathrm{asym}). \tag{12}$$

The perturbation series for the p_T distribution — and therefore R — has been computed to 2nd order in ref. [14]. The total cross section is then written

$$\frac{\mathrm{d}\sigma}{\mathrm{d}p_T^2\,\mathrm{d}y\mathrm{d}M^2}(\mathrm{total}) = \frac{\mathrm{d}\sigma}{\mathrm{d}p_T^2\,\mathrm{d}y\mathrm{d}M^2}(\mathrm{resum}) + \frac{\mathrm{d}\sigma}{\mathrm{d}p_T^2\,\mathrm{d}y\mathrm{d}M^2}(\mathrm{pert}) - \frac{\mathrm{d}\sigma}{\mathrm{d}p_T^2\,\mathrm{d}y\mathrm{d}M^2}(\mathrm{asym}). \tag{13}$$

The "matching" is now manifest: at low p_T the perturbative and asymptotic pieces cancel, leaving the resummed; at high p_T the resummed and asymptotic pieces cancel to 2nd order, leaving the perturbative contribution. The relative error is explicitly of order α_{s}^2, see ref. [11].

At very high p_T the matching prescription breaks down and one must switch back to the perturbative result. This breakdown occurs because $\mathrm{d}\sigma/\mathrm{d}p_T^2\,\mathrm{d}y\mathrm{d}M^2(\mathrm{asym})$

is only known to 2nd order, while $\mathrm{d}\sigma/\mathrm{d}p_T^2\,\mathrm{d}y\mathrm{d}M^2(\mathrm{resum})$ in effect contains all orders in α_s. For example, $\mathrm{d}\sigma/\mathrm{d}p_T^2\,\mathrm{d}y\mathrm{d}M^2(\mathrm{resum})$ introduces terms $\propto \alpha_\mathrm{s}^3(\ln p_T)^5/p_T^2$ that will not be cancelled in the 2nd order expression for $\mathrm{d}\sigma/\mathrm{d}p_T^2\,\mathrm{d}y\mathrm{d}M^2(\mathrm{asym})$. Although such terms are higher order in α_s they become important at large p_T for kinematic reasons. The resummed and asymptotic cross sections depend on parton distributions evaluated at a fixed x, independent of p_T, whereas the parton distributions probed by the perturbative result fall with increasing p_T. Thus, the higher order terms come to dominate at large p_T and one must switch back to the perturbative result. An appropriate value of p_T at which to do this is when when $\mathrm{d}\sigma/\mathrm{d}p_T^2\,\mathrm{d}y\mathrm{d}M^2$ has fallen off to the extent that R is comparable to the total. At that point, the terms being resummed no longer dominate the cross section and at higher p_T the perturbative prediction is more reliable than (13). The switch is done at sufficiently high p_T so that the error incurred is free of large logarithms.

The form factor $W(b)$ contains α_s and parton distributions evaluated at the scale $1/b$, and its evaluation is problematic for $b > 1$ GeV^{-1}. Moreover, one wishes to include the effect of the intrinsic p_T of the partons. Both of these ends are met by replacing

$$W(b) \to W(b_*)\mathrm{e}^{-S_\mathrm{np}(b)} \tag{14}$$

where $b_* = b/\sqrt{1+(b/b_\mathrm{max})^2}$ and $b_\mathrm{max} = 0.5$ GeV^{-1}. The Collins-Soper-Sterman formalism specifies that S_np have a term which depends on $\ln M$ and a term which does not and that the $\ln M$ term does not depend on the colliding hadrons or on the parton x's. However, beyond these constraints S_np is arbitrary and must be extracted from experiment. Ladinsky and Yuan parametrize

$$S_\mathrm{np} = g_1 b\,[b + g_3\,\ln(\tau/\tau_1)] + g_2 b^2\,\ln(M/2M_1), \tag{15}$$

where $\tau = x_1 x_2$ [20]. To fit the ISR p_T distribution from R209, they take $g_1 = 0.11$ GeV^2, $g_2 = 0.58$ GeV^2, $g_3 = -1.5$ GeV^2, $\tau_1 = 0.01$ and $M_1 = 1.6$ GeV. Note that these parameter choices are somewhat different from those in ref. [11, 19].

Momentum distributions presented in the work are computed using a code adapted from ref. [11]. One source of uncertainty in these predictions is the neglect of higher orders in α_s. The difference between the perturbative and matched results at high p_T is one indication of this uncertainty. Further ambiguity arises in our estimate of the intrinsic p_T smearing, which is entirely phenomenological.

Angular Distributions

It is possible to probe the spin structure of the production amplitudes by measuring the angular distribution of the dileptons.

The general form of the angular distribution is

$$\begin{aligned}\frac{\mathrm{d}\sigma}{\mathrm{d}M^2\mathrm{d}y\mathrm{d}p_T^2\mathrm{d}\Omega} &= \frac{3}{16\pi}\frac{\mathrm{d}\sigma}{\mathrm{d}M^2\mathrm{d}y\mathrm{d}p_T^2} \times [1+\cos^2\theta + \frac{A_0}{2}(1-3\cos^2\theta) \\ &+ A_1\sin 2\theta\cos\phi + \frac{A_2}{2}\sin^2\theta\cos 2\phi]\end{aligned} \tag{16}$$

where the angles θ and ϕ are measured in the dilepton rest frame with respect to an arbitrary axis. For calculations with underlying QCD processes, it is convenient to evaluate the A_i in the Collins–Soper frame [21], where the reference axis is the bisector of the beam and (anti) target directions. This choice in some respect minimizes the effect of intrinsic parton transverse momenta.

For the experimental analysis, it is standard to use an alternate parameterization

$$\frac{\mathrm{d}\sigma}{\mathrm{d}\Omega} \sim 1 + \lambda \cos^2\theta + \mu \sin 2\theta \cos\phi + \frac{\nu}{2} \sin^2\theta \cos 2\phi \,. \tag{17}$$

The relationship is simply obtained

$$\begin{aligned} \lambda &= \frac{2 - 3A_0}{2 + A_0} \\ \mu &= \frac{2A_1}{2 + A_0} \\ \nu &= \frac{2A_2}{2 + A_0} \,. \end{aligned} \tag{18}$$

For calculations in perturbative QCD, one embeds the partonic expressions for $A_i \times \mathrm{d}\sigma/\mathrm{d}M^2\mathrm{d}y\mathrm{d}p_T{}^2$ into integrals over parton density functions just as in the previous sections. The Born term involves only zero transverse momentum, and the virtual photon production amplitude vanishes for zero helicity. Thus all of the A_i's are zero and the angular distribution is purely $1 + \cos^2\theta$. For the parton level A_i the leading order (LO) perturbative corrections of order α_s have been calculated through the spin amplitudes in the annihilation and Compton amplitudes. One finds in all cases the relationship $A_0 = A_2$, or equivalently $\lambda = 1 - 2\nu$, such that the θ and ϕ distributions are correlated. Calculations in NLO of order α_s^2 are much more complicated [22], but in general only alter the angular coefficients at the 10% level [23]. However, the correlation above is then violated.

In this study we have calculated the perturbative cross section and amplitudes A_0 and A_1 using the LO expressions (remember at this level $A_0 = A_2$).

$$\begin{aligned} \frac{\mathrm{d}\sigma}{\mathrm{d}M^2\mathrm{d}y\mathrm{d}p_T^2} A_i = {} & \frac{8\alpha^2\tau^2\alpha_\mathrm{s}(\mu)}{27\pi M^6} \int_0^1 \frac{dx_1}{x_1} \int_0^1 \frac{dx_2}{x_2} \delta(x_1x_2 - x_1z_2 - x_2z_1 + \tau) \\ & \times \Big\{ \Big[\sum_k e_k^2 \big(q_k(x_1,\mu)\ \bar{q}_k(x_2,\mu) + (-1)^i (x_1 \leftrightarrow x_2) \big) \Big] \hat{A}_i^{q\bar{q}} \\ & + \Big[\sum_k e_k^2 \big(g(x_1,\mu)(q_k(x_2,\mu) + \bar{q}_k(x_2,\mu)) + (-1)^i (x_1 \leftrightarrow x_2) \big) \Big] \hat{A}_i^{gq} \Big\}, \end{aligned} \tag{19}$$

where $z_{1,2} \equiv [\tau(1+(p_T/M)^2]^{\frac{1}{2}} e^{\pm y}$ are generalizations of (4) for $p_T \neq 0$. To calculate the cross section alone, one replaces the parton-level $\hat{A}_i$ with the parton-level cross section $\hat{\Sigma}$. Expressions for these quantities are:

$$\hat{\Sigma}^{q\bar{q}} = \frac{(M^2-u)^2+(M^2-t)^2}{ut}$$
$$\hat{A}_0^{q\bar{q}} = \frac{M^2-u}{M^2-t} + \frac{M^2-t}{M^2-u}$$
$$\hat{A}_1^{q\bar{q}} = \left[\frac{M^2 s}{ut}\right]^{\frac{1}{2}} \left(\frac{M^2-u}{M^2-t} - \frac{M^2-t}{M^2-u}\right)$$
$$\hat{\Sigma}^{gq} = \frac{(M^2-s)^2+(M^2-t)^2}{-st}$$
$$\hat{A}_0^{gq} = \frac{-u\left[(s+M^2)^2+(M^2-t)^2\right]}{s(M^2-u)(M^2-t)}$$
$$\hat{A}_1^{gq} = \left[\frac{M^2 u}{st}\right]^{\frac{1}{2}} \frac{(M^2-u)^2-2(M^2-t)^2}{(M^2-u)\,(M^2-t)} \tag{20}$$

and one must make the replacement $t \leftrightarrow u$ for the gluon-quark terms when interchanging projectile and target.

Note that the invariants s, t, u, and M^2 are calculated with parton momenta in the annihilation and Compton diagrams, and the $\hat{A}_i$ are given in the Collins–Soper frame. We have used the LO $\alpha_{\rm s}$ values for each parton distribution set used in these calculations, as is appropriate for our LO angular distribution expressions. The scale is taken to be $\mu = M$ in all cases.

One can see from the structure of parton-level amplitudes in Eq (20) how the angular distribution coefficients change as the perturbative contributions grow with p_T. For the $q\bar{q}$ subprocess, one finds the relation

$$\hat{A}_0^{q\bar{q}} = \frac{p_T^2}{p_T^2+M^2}\hat{\Sigma}^{q\bar{q}}. \tag{21}$$

Since this relation holds for all parton momenta, one predicts that A_0 and hence λ will be independent of the parton distribution functions. It will also be independent of energy and rapidity, and exhibit a characteristic function of $w \equiv (p_T/M)^2$. This property was found some time ago [24, 25], and the prediction in the Collins–Soper frame at any fixed y is

$$\lambda^{q\bar{q}} = \frac{2-w}{2+3w}. \tag{22}$$

One sees that as w increases with p_T, the virtual photon polarization state increases in the zero helicity mode. The limiting value as $p_T \to \infty$ is $\lambda = -1/3$, corresponding to a factor of two for the ratio of longitudinal to transverse photon production. There is no corresponding relation for the A_1 amplitude.

A similar analysis for the gq amplitudes does not yield a relation such as Eq. (21). However, one can get an approximate result which only depends on the steeply-rising behavior of the parton distribution functions at small x. If the integral over parton momenta is saturated by the values at the smallest possible x–values, for small rapidity values one samples only at the point $-u = -t = p_T^2 + p_T\sqrt{p_T^2 + M^2}$. The corresponding amplitude relationship is then

$$\hat{A}_0^{gq} \approx \frac{5p_T^2}{M^2 + 5p_T^2}\hat{\Sigma}^{gq}, \tag{23}$$

which leads to a new characteristic function

$$\lambda^{gq} = \frac{2 - 5w}{2 + 15w}. \tag{24}$$

These relations were first found in the Gottfried–Jackson frame [25] for y-integrated quantities, but apply in the form above in the Collins–Soper frame at fixed y [26] sufficiently small such that $\hat{A}_1 \approx 0$. One can see that the characteristic functions are related by a rescaling of w by a factor of five between the $q\bar{q}$ and the gq subprocesses.

Our normalized $A_i's$ and calculated λ, μ, and ν values are valid only in a region of transverse momentum p_T large enough that the perturbative terms may be expected to dominate the amplitudes. At lower values of p_T, the soft gluon resummation technique must be used to calculate the p_T-dependence of the cross section. As noted by Chiapetta and Le Bellac [27], the A_i terms do not enter into the resummation, since only the part proportional to $1 + \cos^2\theta$ is able to combine with the soft gluon resummation amplitude. Thus at low p_T one should simply replace the perturbative cross section with the resummed differential cross section, and use this factor to normalize the A_i's integrated over parton distributions. It is unclear, however, how to determine in general where the perturbative region begins. At the Fermilab and CERN fixed-target and ISR energies which provide the data presently available for p_T distributions, it appears that the perturbative terms will dominate only when $p_T > M$. On the other hand, calculations for W and Z production at SPS and Tevatron energies indicate that the perturbative contributions are dominant already when $p_T \leq M/2$. Due to this uncertainty, we present for this study only the perturbative cross section and the perturbative A_i values, plus the calculated λ and μ values. In regions of small p_T, one should use the resummed cross sections to renormalize the A_i and recalculate the λ and μ values, but the crossover point in p_T must be determined independently for each collider energy and dilepton mass.

Nuclear Effects

We now comment on possible nuclear modification in the Drell–Yan process. On naive geometrical grounds, one expects that the cross sections differential in M and y in central ion-ion collisions increase with nuclear mass by a factor $\propto A^{4/3}$ relative to the $N-N$ cross section. Any modification of the parton distributions in the target and projectile nuclei will modify this dependence. In particular, one expects parton shadowing to be very important in the small x range probed by midrapidity Drell–Yan production at the RHIC and, especially, at the LHC. Shadowing can reduce the A dependence of the cross section relative to the expected increase by as much as a factor of $\sim A^{1/3} \sim 6$ in Au–Au collisions. Such a dramatic suppression would be larger than the combined uncertainties in our $N-N$ cross section calculations. It will nevertheless be crucial to measure the $N-N$ rates at RHIC and LHC to study shadowing and other such nuclear effects.

Initial state parton scattering has been measured in Drell–Yan studies of hadron–nucleus collisions. This scattering does not appreciably affect rapidity and mass distributions, but can modify the p_T spectrum. Specifically, initial state scattering broadens the transverse momentum distribution in a nuclear target relative to a hadron target, corresponding to an increase $\propto A^{1/3}$ in $\langle p_T^2 \rangle$. This broadening is measured experimentally. Note that it is because of this effect that we have not compared p_T calculations to nuclear target data.

COMPARISON WITH DATA

In this section we compare calculations to recent experiments in order to illustrate the level of agreement of the QCD calculations with data. We have chosen not to optimize the calculations, *e.g.,* by choosing the scales via some prescription [28]. Instead we vary the regularization scheme and scales in order to determine the level of uncertainty in the prediction. We exclude data on nuclear targets from our analysis, because nuclear effects are not addressed in this work. Even so, our comparisons with data are not exhaustive and we apologize to our experimental colleagues for our incompleteness.

Mass Distributions

A comparison of the perturbative calculations to the data from fixed–target experiments is discussed in detail by Rijken and van Neerven [6]. The overall feature of most of the fixed–target data for $\mathrm{d}\sigma/\mathrm{d}M$ is described by the Born term multiplied by a K factor in the range $1 < K < 2$. The reason for this 'factorization' is understood [16, 17], and the goal of perturbative calculations of the mass spectrum is to calculate the K factor. One finds that the $\mathcal{O}(\alpha_\mathrm{s})$ calculation can account for $50-75\%$ of the experimental K factor. It is not clear whether K can be calculated entirely using perturbation theory. As we discuss below the situation improves for the data at highest energies now available.

In addition Rijken and van Neerven calculate the NNLO, $\mathcal{O}(\alpha_\mathrm{s}^2)$, contributions from soft and virtual gluons $(S+V)$ to the double-differential cross section $\mathrm{d}\sigma/\mathrm{d}M\mathrm{d}x_F$ and study the validity of this approximation at the $\mathcal{O}(\alpha_\mathrm{s})$ where the exact result is known. They find the approximation valid that at the fixed–target energies for $\sqrt{\tau} = M/\sqrt{s} > 0.3$. Assuming this to be the case also for the NNLO contribution, they conclude that part of the discrepancy between the data and the $\mathcal{O}(\alpha_\mathrm{s})$ result can be attributed to the $S+V$ contributions [6].

We have extended the comparison in ref. [2] to the mass dependence of the double differential cross section, $\mathrm{d}\sigma/\mathrm{d}M\mathrm{d}x_F$, measured in the FNAL E772 experiment at 800 GeV ($\sqrt{s} = 38.8$ GeV) [29] and in the CERN ISR experiment R209 [30] at $\sqrt{s} = 44$ and 62 GeV. In Fig. 1 we show the mass distributions from the E772

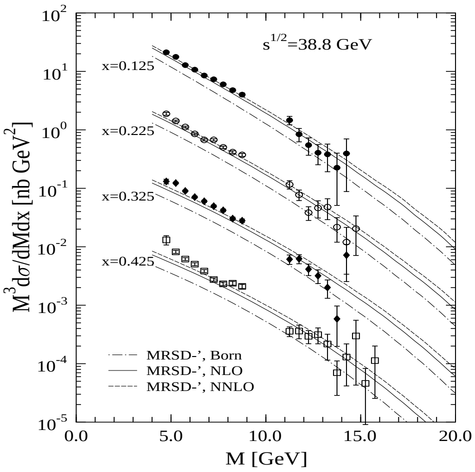

Figure 1: The calculated [6] scaling function $M^3 \mathrm{d}\sigma/\mathrm{d}M\mathrm{d}x$ for four values of Feynman $x_F \equiv x$ compared to $pp \to \mu^+\mu^-$ data at $\sqrt{s} = 38.8$ GeV from FNAL E772 [29]. Born, $\mathcal{O}\alpha_\mathrm{s}$ and $\mathcal{O}\alpha_\mathrm{s}^2$ cross sections are indicated by the dash-dotted, solid and dashed curves. Next-to-leading corrections are obtained in the $S{+}V$ approximation.

experiment [29] at four different x_F values for the pair, $x_F = 0.125$, 0.225, 0.325, and 0.425 together with results from a calculation in the $\overline{\mathrm{MS}}$ sceme using the MRS D$-'$ parton distributions [7, 8]. We take the scale μ equal to the mass of the pair, as discussed later. At low x_F the data and the perturbative calculation are in fairly good agreement. The calculated cross section is slightly below the data at the lower end of the measured mass range and slightly above at the higher end. With increasing x_F the difference between the data and the calculated results increases at the low-mass end of the spectrum.

At this energy the validity of the $S{+}V$ approximation for the $\mathcal{O}(\alpha_\mathrm{s})$ contribution is ~ 10 % at $M = 20$ GeV and decreases to $\sim 50\%$ for $M = 3$ GeV, the approximate result being larger than the exact calculation. If the pattern is the same for the second order corrections, the complete NNLO calculation would deviate from the NLO results even less than shown in Fig. 1.

In Figs. 2 and 3 the data on $\mathrm{d}\sigma/\mathrm{d}M\mathrm{d}x_F$ measured at CERN ISR [30] at $\sqrt{s} = 44$ and 62 GeV and at $x_F = 0$ are compared to calculations. At both energies the Born term alone reproduces the continuum data between the J/ψ and the Υ. For the large mass region the corrections improve the comparison. At $\sqrt{s} = 44$ GeV only results for the MRS D$-'$ structure functions and for the scales set to the mass of the pair, $\mu_F = \mu_R = M$, are shown. The NNLO correction calculated in the soft plus virtual gluon approximation is seen to be clearly smaller than the NLO correction. Its precise magnitude cannot, however, be trusted with decreasing values of $\tau = M^2/s$. At $\sqrt{s} = 62$ GeV the $S + V$ contribution in the NLO term is twice the complete result at small masses. This implies that the uncertainty in the NNLO correction in the mass (or τ) range of interest in our extrapolations to higher energies is of the order of the correction itself. Fortunately the correction is small, and in the following we choose to show results with NLO corrections only. We should like to emphasize that all the available information on the NNLO contributions, including the full calculation for the rapidity integrated and total cross sections, indicate that

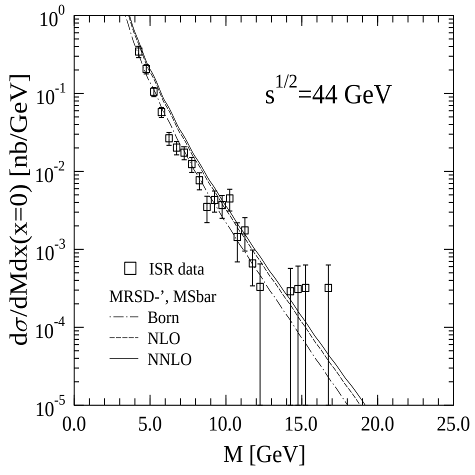

Figure 2: Same as Fig. 1 compared to ISR R209 data [31] at $\sqrt{s} = 44$ GeV.

the corrections add at most 20 % to the NLO corrected cross sections.

At $\sqrt{s} = 62$ GeV we show results for MRS D$-'$, D0$'$, and the GRV HO parton distribution sets [7, 8, 9] with $\mu_F = \mu_R = M$ and study the scale dependence in the case of MRS D$-'$ set using the NLO results. It is not surprising that the different sets give very similar results since they have been determined from data which covers or is close to the kinematic region we consider here. The differences are too small to discriminate between any of these sets. Varying the scale introduces a larger change in the results at this energy. Specifically, an increase of the scale reduces the calculated result. Nevertheless, for $M \leq 10$ GeV the change is inconsequential and we choose to present our extrapolations using $\mu_F = \mu_R = M$.

Transverse Momentum Distributions

Transverse momentum spectra computed at next-to-leading order following Arnold and Kauffman [11] are compared to data from ISR experiment R209 $\sqrt{s} =$ 62 GeV [31] in Fig. 4. The nonperturbative parameters employed here (15) were obtained using a leading-order calculation in ref. [20] by fitting data from this experiment and FNAL experiment E288 at $\sqrt{s} = 27.4$ GeV [32]. Our NLO calculations are performed using the MRS D$-'$ parton distributions at the scale M.

We compare calculations to Fermilab experiment E772 at $\sqrt{s} = 38.8$ GeV in Fig. 5. The data in fig. 5 are averaged over the range $0.1 < x_F < 0.3$ for the three different mass bins shown. Our calculations at this lower energy are in excellent agreement with the shape of the momentum spectra. In particular, the variation of the p_T distributions with mass agrees with data. However, present calculations overpredict the integrated rate by $\sim 50\%$. In view of this disagreement, we present RHIC and LHC predictions for transverse momentum distributions normalized to the total cross section.

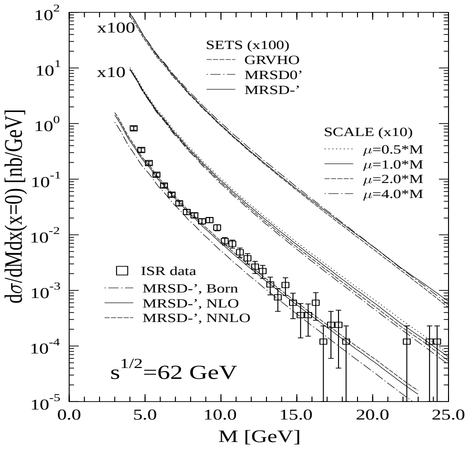

Figure 3: Same as Fig. 1 compared to ISR R209 data [31] at $\sqrt{s}$ = 62 GeV. Additional curves multiplied by 10 and 100 indicate the dependence on scale and parton distributions.

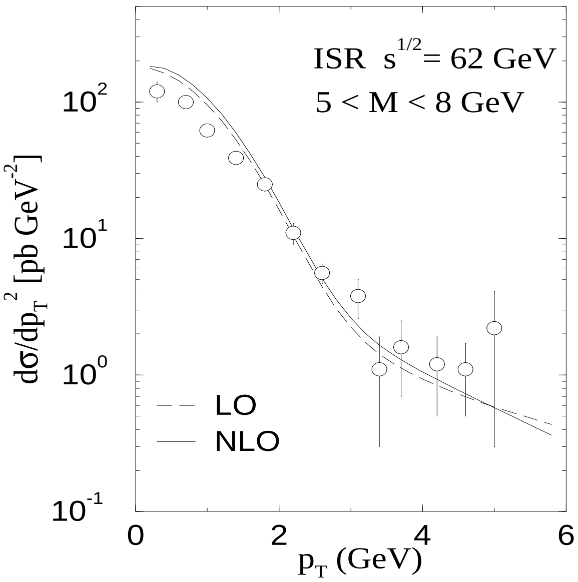

Figure 4: The rapidity-integrated cross section $\mathrm{d}\sigma/\mathrm{d}p_T^2$ in the mass range $5 < M < 8$ GeV at $\sqrt{s} = 62$ GeV compared to data from CERN R209. Note that the normalization of the calculation agrees with that of the data.

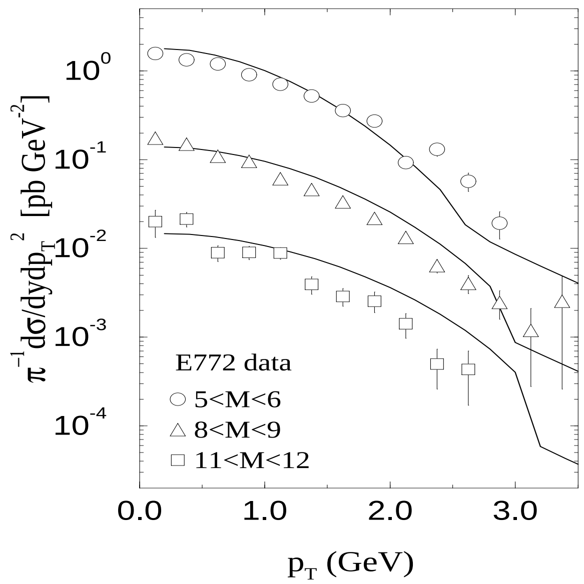

Figure 5: The invariant cross section for $pp \to \mu^+\mu^-$ at $\sqrt{s} = 40$ GeV are compared to measurements from FNAL E772. The circles, triangles, squares and the nearby curves represent data and calculations integrated over the three mass bins $5 < M < 6$ GeV, $8 < M < 9$ GeV and $11 < M < 12$ GeV, respectively. Data and calculations are averaged over the range $0.1 < x_F < 0.3$. Calculations are rescaled by an *ad hoc* overall factor of 0.63.

Angular Distributions

The only data presently available on the angular distribution coefficients are from fixed-target $\pi-N$ experiments at Fermilab E615 [33] and CERN NA10 [34, 26]. These experiments cover similar kinematic regions, roughly $\sqrt{s} \approx 20$ GeV, $4 \lesssim M \lesssim 8$ GeV, and $0 \lesssim p_T \lesssim 3$ GeV. The general trend of the data produces values of λ which are close to unity and almost independent of p_T, μ close to zero, and ν increasing with p_T. The perturbative predictions are in agreement with the μ and ν values, but fall below the λ values at the highest p_T. This behavior can be brought into agreement with data via the procedure of soft gluon resummation, which also appears necessary to reproduce the magnitude of the p_T dependent cross section [27]. However, this procedure then brings the predictions for ν down close to zero, in significant disagreement with data. The overall result is a violation of the relation $1 - \lambda - 2\nu = 0$ in either the perturbative or resummed predictions. This relation should hold exactly at LO QCD and has slightly positive contributions from the higher order corrections [23]. The data show definite negative values, which are difficult to understand in a QCD calculation. In fact, this has led to attempts to fit this data with models incorporating initial state correlations of color fields which lead to spin correlations [35]. A general conclusion must be drawn from the $\pi - N$ data that the angular distribution results are not well understood within perturbative QCD.

NUMERICAL RESULTS FOR RHIC AND LHC ENERGIES

We now turn to our predictions for RHIC and LHC energies and their uncertainties.

Mass and Rapidity Distributions

Mass distributions for p-p collisions are presented in Tables 1–4 and Figs. 6–11. In fig. 6 we show the scale dependence at $\sqrt{s} = 200$ (a) and 5500 GeV (b) for different fixed values of the pair mass as a function of μ/M. Not surprisingly, the dependence is stronger for smaller masses. The peak at small scale for $M = 4$ GeV is caused by the increase of $\alpha_{\rm s}(M)$ as M approaches the $\Lambda_{\rm QCD}$. Perturbative calculations are not expected to be valid at such a small scale. For large values of the scale the dependence of the results is weak, although $\mathrm{d}\sigma/\mathrm{d}\mu$ does not vanish, as would be the case if σ were locally independent of μ. We take the scale to be M for our RHIC and LHC predictions. These results imply that the uncertainty in these prediction due to the scale ambiguity is $\sim 25\%$.

The scheme dependence of the double differential cross section is shown in Figs. 7 and 8 for $\sqrt{s} = 200$ GeV and 5.5 TeV. Observe that the scheme dependence of the parton distributions alone leads to a 10% difference in the Born terms. When the $\mathcal{O}(\alpha_{\rm s})$ corrections are added the difference between the schemes decreases. This difference is smaller than the calculated correction, as expected since the scheme dependence of the cross section is of higher order. The difference of the Born terms

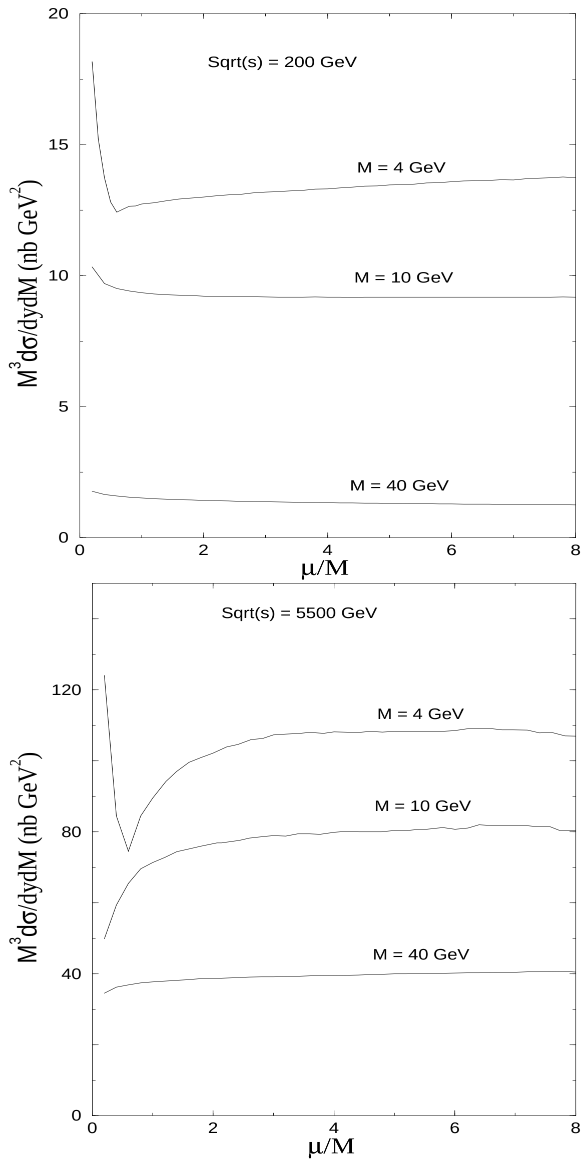

Figure 6: The scale dependence of the scaled cross section $M^3 \mathrm{d}\sigma/\mathrm{d}M\mathrm{d}y$ at RHIC (a) and LHC (b) energies in the $\overline{\mathrm{MS}}$ scheme at $\mathcal{O}\alpha_s$. The scales are chosen to be equal, $\mu_R = \mu_F = \mu$.

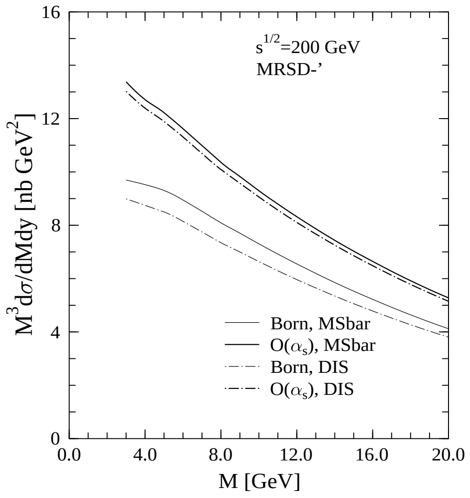

Figure 7: The scheme dependence of the $\mathcal{O}(\alpha_s)$ cross section at $\sqrt{s} = 200$ GeV for the MRS D$-'$ parton distribution set.

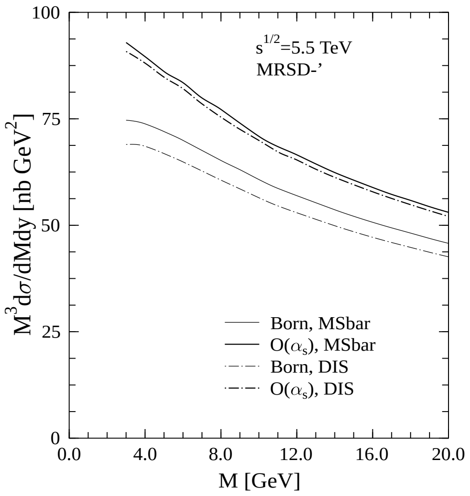

Figure 8: Same as in Fig. 2 but for the LHC energy, $\sqrt{s} = 5.5$ TeV.

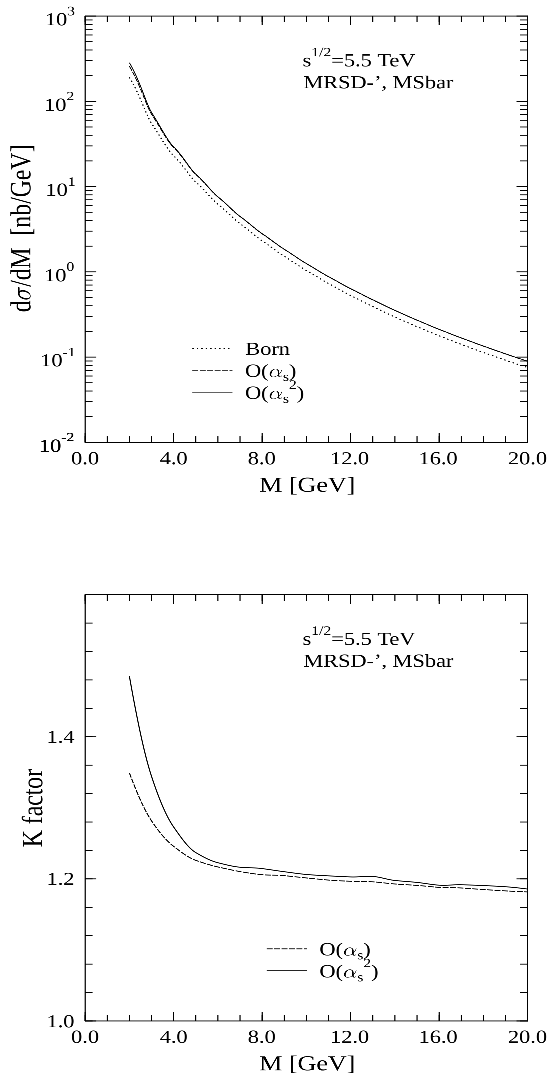

Figure 9: Rapidity integrated cross section $\mathrm{d}\sigma/\mathrm{d}M$ (a) and the theoretical K-factor (b) (see text for the definition) at $\sqrt{s} = 5.5$ TeV. In (a) the dotted curve shows the Born term, dashed curve the $O(\alpha_\mathrm{s})$, and the solid curve the $O(\alpha_\mathrm{s}^2)$ result. In (b) the dashed curve shows the $O(\alpha_\mathrm{s})$ and the solid curve the $O(\alpha_\mathrm{s}^2)$ K-factor.

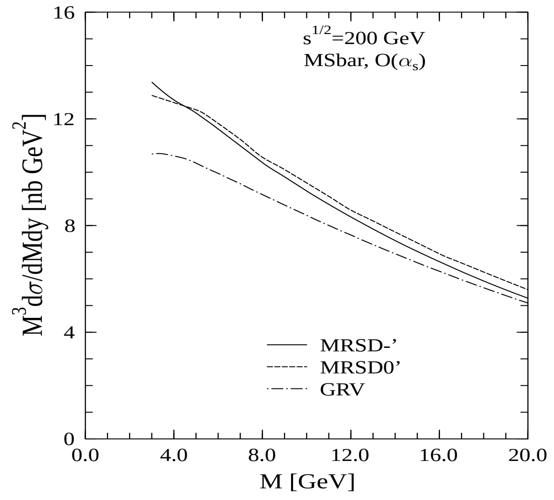

Figure 10: The cross section $\mathrm{d}\sigma/\mathrm{d}M\mathrm{d}y$ at $y = 0$ as a function of M for different parton distribution functions for the LHC energy, $\sqrt{s} = 5.5$ TeV. Solid curve shows the result for MRS D$-'$ set, dash-dotted curve for the GRV HO set and dashed curve for the MRS D$0'$ set.

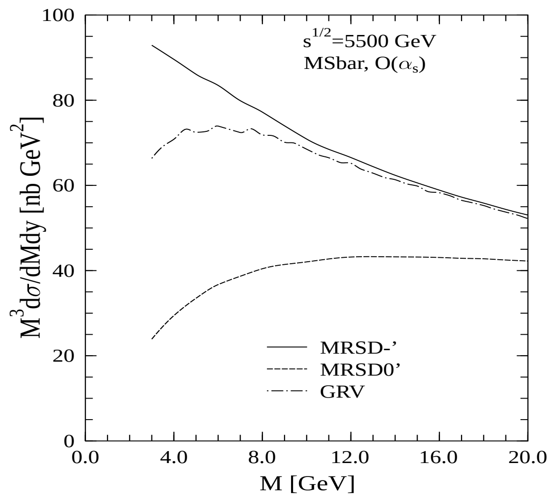

Figure 11: Same as Fig. 10, except for the RHIC energy, $\sqrt{s} = 200$ GeV.

is expected to be of the order α_s. This seems to be the case even though the difference is smaller than the $\mathcal{O}(\alpha_s)$ corrections.

As mentioned earlier, the $\mathcal{O}(\alpha_s^2)$ corrections to $\mathrm{d}\sigma/\mathrm{d}M\mathrm{d}y$ have recently been studied [5, 6] but are not yet completely known. It has been shown [3] that at the present fixed–target energies the $\mathcal{O}\alpha_s$ corrections are dominated by the soft and virtual gluon corrections. Here we are interested in collisions at larger values of $\sqrt{s}$ and smaller masses, down to 2–3 GeV. It seems that the soft plus virtual gluon approximation breaks down in this domain. However, the full $\mathcal{O}(\alpha_s^2)$ result is known for the rapidity integrated cross section $\mathrm{d}\sigma/\mathrm{d}M$ [4]. We show the results at the LHC energy, $\sqrt{s} = 5.5$ TeV, both for the cross section, Fig. 9a, and the theoretical K factor Fig. 9b. Above $M = 4$ GeV the second order corrections are a small fraction of the first order corrections and the perturbation theory seems to converge rapidly. At smaller values of mass the perturbative results become less reliable but even at $M = 2$ GeV the second order correction is not more than $\sim 10\%$ of the Born term. It seems that extending the perturbative calculations down to this mass region is still meaningful with an uncertainty of $\lesssim 25\%$.

The parton distribution functions are quite well known for $x \gtrsim 10^{-2}$ and recent parametrizations given by different groups [7] are essentially equivalent. We give the results at $\sqrt{s} = 200$ GeV and 5.5 TeV for three different sets: MRS D0$'$, D$-'$ [8], and GRV HO [9]. These sets differ from each other for $x < 10^{-2}$ and essentially span the interval compatible with the present HERA data. The D0$'$ set goes slightly below the data and the MRS D$-'$ set slightly above.

Fig. 10 shows the mass spectrum for dileptons at RHIC energy. The differences in the results for different parton distributions are $\lesssim 20\%$. For the LHC energy the situation is much worse, as shown in Fig. 11. The parton distributions are now probed down to $x = M/\sqrt{s} \sim 10^{-4}$ and the uncertainty in the cross section at $M = 3$ GeV is almost a factor of 4 decreasing to a factor less than 2 at 10 GeV.

Rapidity distributions at the RHIC energy are presented for fixed pair mass in Fig. 12 for the MRS D$-'$ parton distribution set. The interesting feature is the increase of the cross section at the smaller mass values as the rapidity increases from 0 to ~ 3. As is seen from Eq. (4), x_1 increases and x_2 decreases with increasing y. The growth of the cross section reflects the faster increase of $x_2\bar{q}(x_2, \mu_F)$ with decreasing x_2 as compared to the decrease of $x_1 q(x_1, \mu_F)$ with increasing x_1. This depends on the detailed shape of the parton distributions at low x and, *e.g.,* for D0$'$ set the cross section is almost flat in the central rapidity region.

At $\sqrt{s} = 5.5$ TeV the increase of cross section with y occurs up to higher values of mass. For $M = 3$–10 GeV the cross section peaks at $y \sim 4$ where its value is typically twice that at $y = 0$ for the MRS D$-'$ set.

Transverse Momentum Distributions

Transverse momentum distributions for p-p collisions at the RHIC and LHC heavy-ion energies are shown in Figs. 13–19 normalized to the p_T-integrated cross section. To understand some of the features of these spectra, we focus on the RHIC results, Figs. 13–17. Fig. 13 shows $\rho(p_T)$, the normalized p_T distribution calculated at next-to-leading order for $M = 4$ GeV and $y = 0$. The normalization factor is

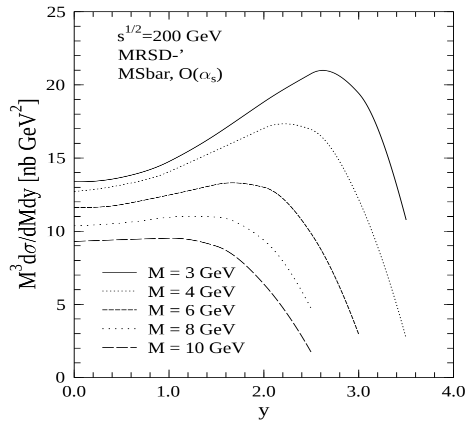

Figure 12: The cross section $\mathrm{d}\sigma/\mathrm{d}M\mathrm{d}y$ at fixed values of M as a function of y for the RHIC energy, $\sqrt{s} = 200$ GeV.

the p_T integrated cross section $\mathrm{d}\sigma/\mathrm{d}y\mathrm{d}M$. The dashed curve is the perturbative prediction valid at high p_T, while the solid thin curve is the matched total cross section (13). Fig. 14 shows the leading order result at the same energy. Observe that the difference between the matched and perturbative curves at high momentum is larger for the LO calculation compared to the NLO one.

Our prediction — the thick solid curve in Fig. 13 — switches between the matched and perturbative solutions, as discussed earlier. Although the matched result (13) formally applies at all momenta, it is not trustworthy at high p_T where the remainder R (dash-dotted curve) exceeds the total matched cross section. The difference between the matched and perturbative results is higher order in α_s; one can regard this difference as a measure of the uncertainty introduced by our truncation of the perturbation series. Observe that this uncertainty is quite small, as we emphasize in Fig. 15 by plotting the results with linear axes.

To illustrate how the matching works, we show the resummed, asymptotic and perturbative components of the matched solution (13) individually in Fig. 16. We see explicitly that the divergent asymptotic part (dash-dotted curve) dominates the perturbation series (thin solid curve) at low p_T. These contributions cancel at low p_T, so that the matched cross section is determined by the resummed result (10,11).

In Fig. 17 we show the p_T spectrum at RHIC for $M = 10$ GeV. The effect of switching is smaller at the higher mass scale. Figs. 18 and 19 show the p_T spectrum at LHC for $\sqrt{s} = 5.5$ TeV, $y = 0$ and $M = 4$ and 10 GeV at next-to-leading order. The matched expression is valid for the entire region $p_T \leq 2M$; switching is unnecessary in this range.

Angular Distributions

For the calculations of angular coefficients in Eqs. (16) and (17) the default parton distribution functions are the MRS D$-'$. We have used fixed-y values mainly at zero, but also up to maximum allowed by kinematics in some cases. We study

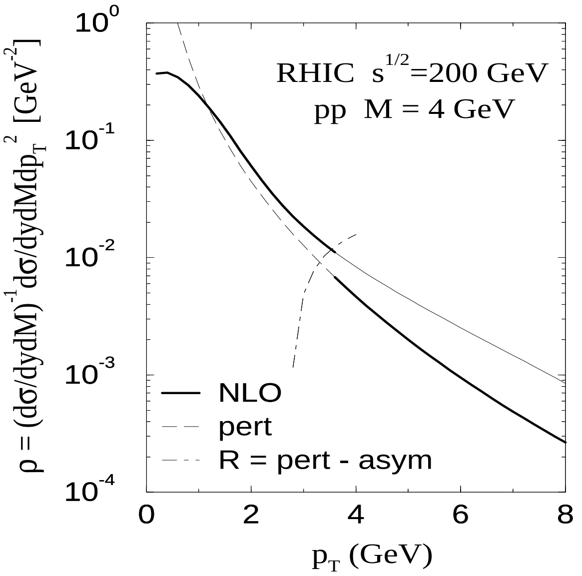

Figure 13: $\rho(p_T) = (\mathrm{d}\sigma/\mathrm{d}y\mathrm{d}M\mathrm{d}p_T^2)/(\mathrm{d}\sigma/\mathrm{d}y\mathrm{d}M)$, normalized transverse momentum spectrum (thick, solid curve) computed at next-to-leading order are shown for RHIC at $\sqrt{s} = 200$ GeV, $y = 0$, and $M = 4$ GeV. The dashed curve is the perturbative prediction valid at high p_T, while the solid thin curve is the matched asymptotic expansion that applies only at low p_T. The matched solution is not trustworthy at p_T's where the remainder R (dash-dotted curve) exceeds to the total matched cross section.

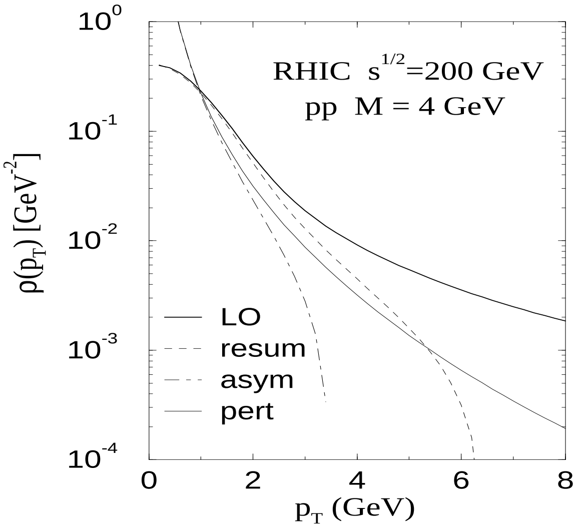

Figure 14: Same as Fig. 13, but for a leading order calculation. All contributions to Eq. (13) are shown explicitly for comparison to the NLO result in Fig. 16.

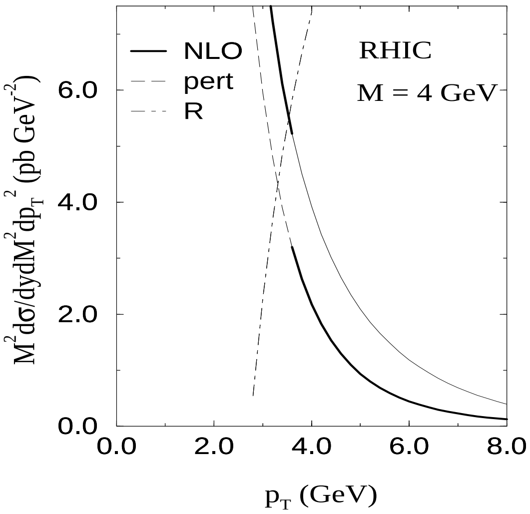

Figure 15: The cross section $\mathrm{d}\sigma/\mathrm{d}y\mathrm{d}M^2\mathrm{d}p_T^2$ from Fig. 13 plotted without the normalization and with linear axes to exhibit the true magnitude of the discontinuity incurred by switching.

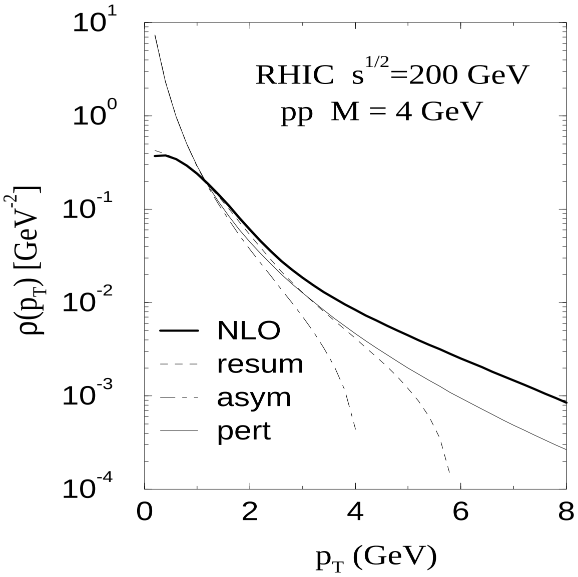

Figure 16: Same as Fig. 13, but showing all the components of the matched solution individually.

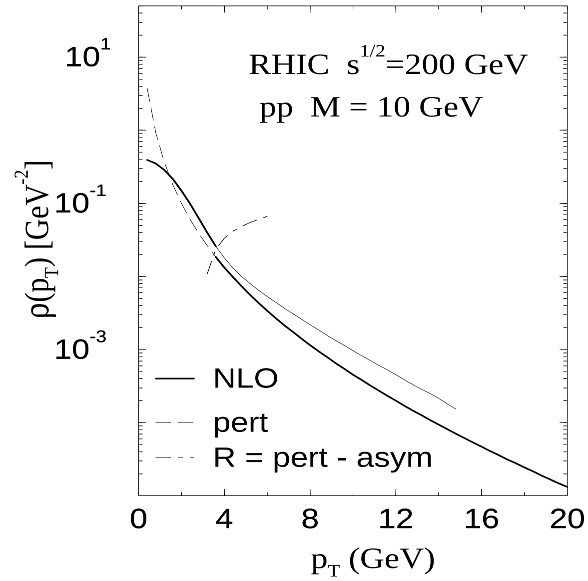

Figure 17: Normalized p_T spectrum at RHIC for $M = 10$ GeV. The effect of switching is smaller at the higher mass scale.

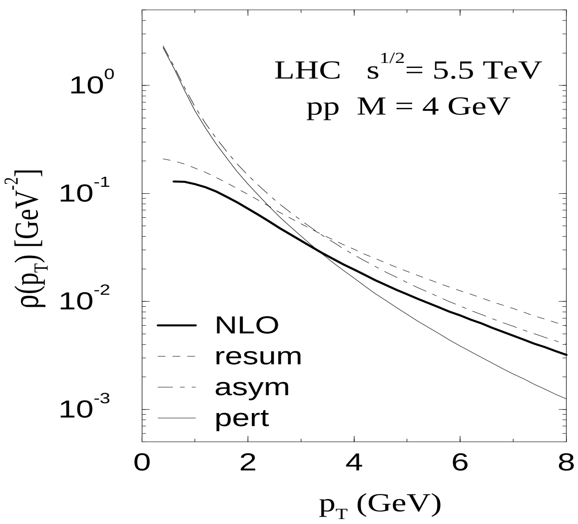

Figure 18: Normalized p_T spectrum at LHC for $\sqrt{s} = 5.5$ TeV, $y = 0$ and $M = 4$ GeV at next-to-leading order. Switching is not necessary for $p_T \leq 2M$.

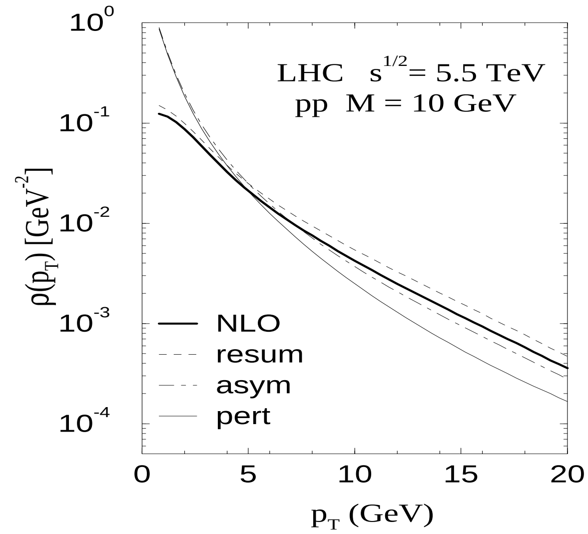

Figure 19: Same as Fig. 18 for $M = 10$ GeV.

the mass range $3 \leq M \leq 30$ GeV with $0 \leq p_T \leq 2M$ in each case.

Fig. 20 shows the λ coefficient at RHIC energy for the default values. As expected, it decreases with increasing p_T and approaches a minimum value of $-1/3$ for large p_T, and scales with p_T/M as predicted by either the $q\bar{q}$ (exact) or gq (approximate) subprocesses. The small scaling violations are an indication that the dominant subprocess must be gq, as one might expect in a p-p interaction. This is verified by separate calculation of the subprocess contributions. We have also verified that the predicted λ values are approximately independent of both $\sqrt{s}$ and the choice of structure function.

All of these calculations were done at $y = 0$, where μ is consistent with zero, as expected from the target-projectile interchange symmetry. At large y, however, we expect to see significant deviations from the simple scaling predictions. Fig. 21 shows the λ and μ values for several rapidities. We see that as the μ parameter becomes nonzero, a corresponding nonuniversal behavior sets in for the λ curves. The corresponding calculations at LHC energy are shown in Fig. 22, where much larger rapidities can be reached. In Fig. 23 we show the corresponding M–dependence at $y = 5$ for LHC. Clearly, no universal scaling appears, as exhibited by the same calculations as a function of p_T/M in Fig. 24.

At low p_T, all of these calculations will be modified by the soft gluon resummation procedure. In general, one would expect $\lambda \approx 1$ and $\mu \approx 0$ for p_T-values up to the point where the perturbative cross section becomes dominant. As an example, we calculate λ and μ at $\sqrt{s} = 38.8$ GeV, where the E772 experiment has measured the p_T distributions [29]. In Fig. 25 we compare their data with the LO perturbative

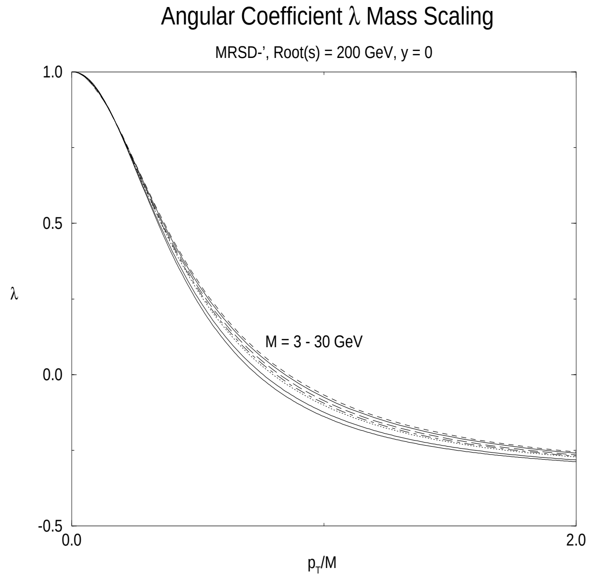

Figure 20: Angular coefficient λ scaling with p_T/M.

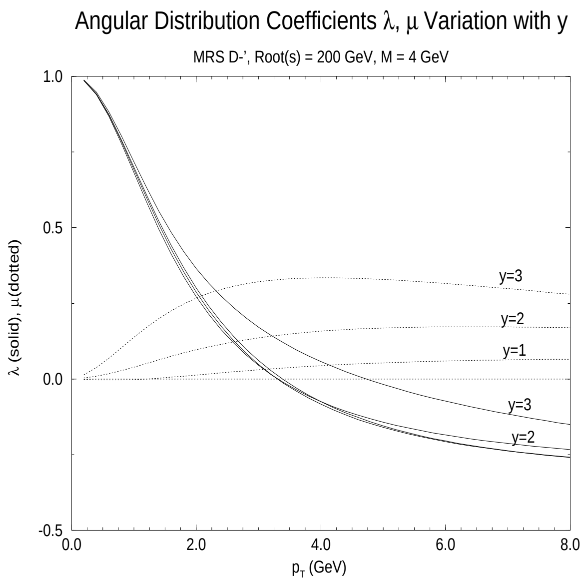

Figure 21: Angular coefficients λ and μ variation with rapidity at $\sqrt{s} = 200$ GeV.

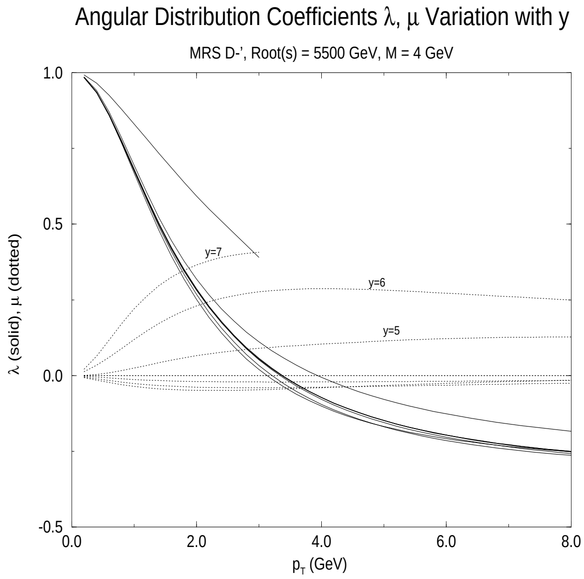

Figure 22: Same as Fig. 21 for $\sqrt{s} = 5500$ GeV.

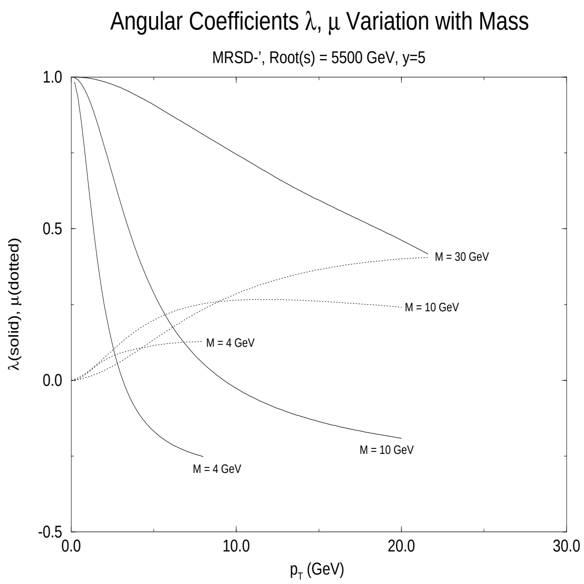

Figure 23: Angular coefficients λ and μ variation with M at large rapidity.

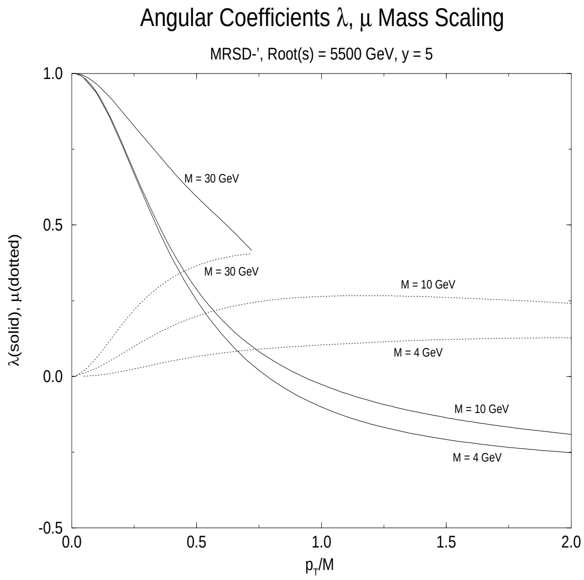

Figure 24: Angular coefficients λ and μ violation of M scaling at large rapidity.

calculations. As expected, the low-p_T region shows the perturbative divergences, the intermediate-p_T region is underestimated by the perturbative terms, and there is some evidence that the data is being matched by the perturbative calculation as p_T approaches values near M. We assume that a proper resummation procedure would match the data at low-p_T and simply rescale the perturbatively-calculated A_i with the ratio of measured to perturbative cross sections at each p_T. Shown in Fig. 26 are the λ and μ coefficients for each case. One sees that at low-p_T the resummation-corrected values remain closer to the uncorrected Born term predictions, *i.e.,* $\lambda = 1,\ \mu = 0$. Since the p_T values at which the perturbative calculations become dominant must be separately determined for each energy and mass value, we simply tabulate the perturbative cross section and the corresponding A_0 and A_1 values for this study at the appropriate RHIC and LHC energies. For each individual case at low p_T, one must then rescale the A_i with the ratio of perturbative cross section to resummed (or experimental) cross section values, and then recalculate the λ and μ parameters.

COMMENTS AND CONCLUSIONS

We have presented perturbative QCD calculations of the Drell-Yan process relevant to experiments with heavy ions at future high-energy colliders. The applicability of our perturbative calculations has also been addressed. In the energy range where experimental results are presently available, the calculations and the data agree to a level of $\sim$ 30% or better. In the high energy domain, $\sqrt{s} \gtrsim 200$ GeV, the perturbative series seems to converge well even down to pair mass of $\sim$2–3

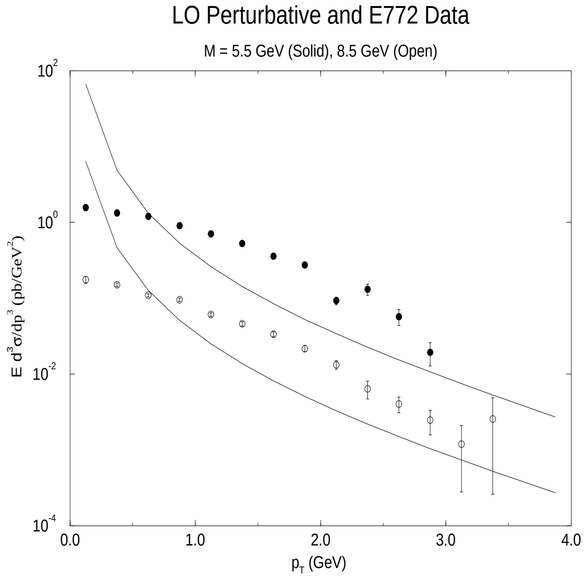

Figure 25: LO perturbative p_T dependence compared with E772 results.

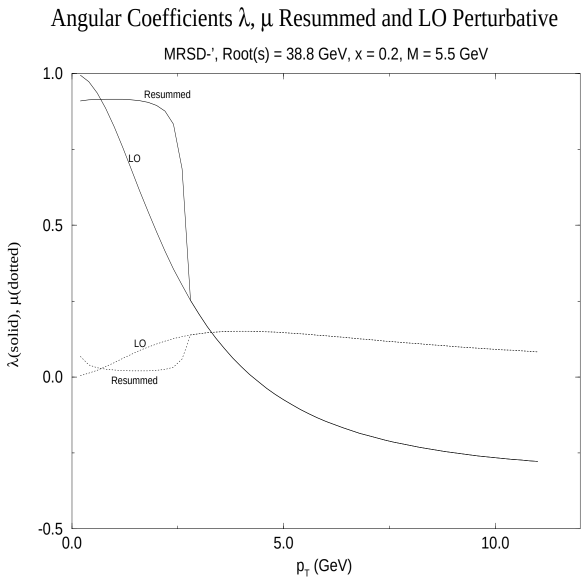

Figure 26: Angular coefficients λ and μ with resummation corrections at low p_T.

GeV with a NNLO contribution of the order of 10% in the rapidity integrated cross section, $d\sigma/dM$. The dependence on the factorization scheme and on the factorization and renormalization scales is not strong except for the smallest considered values of the pair mass, where we estimate the uncertainty to be ~20–30%.

At LHC energy the most serious uncertainty arises from the uncertainty in the parton distribution functions in the small$-x$ region. Different sets which are not ruled out by the present HERA data lead to estimates which differ by a factor of 3–4 for $M \sim 3$ GeV. Since a large pair rapidity indicates a small x for one of the incoming partons, the uncertainty in the parton distributions shows up also in the rapidity dependence of pairs. For the MRS D0$'$ set the rapidity distribution is flat in the central region but for the MRS D$-'$ it first increases with increasing y before the decrease at the phase space boundary.

From the cross sections for a hard process in a nucleon-nucleon interaction the number of such processes in a nucleus-nucleus collision can be obtained by multiplication with the overlap function for the colliding nuclei as defined in [36]. This approach presumes that factorization holds also for nuclear collisions. It also neglects the dependence of the shadowing of parton distributions on the local amount of overlap in the transverse plane. It should be kept in mind that further studies are needed on the shadowing and on the validity of the factorization assumption, especially for this relatively low-mass region of pairs in which we are interested.

Acknowledgements

We are grateful to W.L. van Neerven and P.J. Rijken for the programs of the $d\sigma/dM$ and $d\sigma/dMdy$ cross sections, to P.L. McGaughey for providing the E772 data and to R. Vogt for discussions and helpful comments.

References

[1] S. D. Drell and T. M. Yan, Phys. Rev. Lett. **25** (1970) 316.

[2] W. L. van Neerven, this volume.

[3] K. Kajantie, J. Lindfors and R. Raitio, Phys. Lett. **74B** (1978) 384; J. Kubar-Andre and F. E. Paige, Phys. Rev. **D19** (1979) 221; G. Altarelli, R. K. Ellis and G. Martinelli, Nucl. Phys. **B157** (1979) 461; J. Kubar, M. le Bellac, J. L. Munier and G. Plaut, Nucl. Phys. **B175** (1980) 251; B. Humpert and W. L. van Neerven, Nucl. Phys. **B184** (1981) 225.

[4] R. Hamberg, W. L. van Neerven and T. Matsuura, Nucl. Phys. **B359** (1991) 343; W. L. van Neerven and E.B. Zijlstra, Nucl. Phys. **B382** (1992) 11.

[5] T. Matsuura and W. L. van Neerven, Z. Phys. **C38** (1988) 623; T. Matsuura, S. C. van der Marck and W. L. van Neerven, Nucl. Phys. **B319** (1989) 570; Phys. Lett. **211B** (1988) 171.

[6] P. J. Rijken and W. L. van Neerven, University of Leiden preprint, INLO-PUB-14/94.

[7] H. Plothow-Besch, Comp. Phys. Comm. **75** (1993) 396.

[8] A. D. Martin, W. J. Stirling and R. G. Roberts, Phys. Lett. **306B**, 145 (1993);

[9] M. Glück, E. Reya and A. Vogt, Z. Phys. **C53** (1992) 651.

[10] ZEUS Collaboration, M. Derrick et al., Phys. Lett. **316B** (1993) 412.

[11] P. Arnold and R. Kauffman, Nucl. Phys. **B349** (1991) 381.

[12] R. L. Thews, Phys. Lett. **100B** (1981) 339.

[13] K. Kajantie and R. Raitio, Nucl. Phys. **B139** (1978) 72; R. K. Ellis, G. Martinelli and R. Petronzio, Phys. Lett. **104B** (1981) 45; R. K. Ellis, G. Martinelli and R. Petronzio, Nucl. Phys. **B211** (1983) 106.

[14] P. Arnold and M. H. Reno, Nucl. Phys. **B319** (1989) 37; [Erratum **B330** (1990) 284]; P. Arnold, R. K. Ellis and M. H. Reno, Phys. Rev. **D40** (1989) 912; R. Gonsalves, J. Pawlovski, and C.-F. Wai, Phys. Rev. **D40** (1989) 2245.

[15] Yu. L. Dokshitzer, D. I. Dyakonov and S. I. Troyan, Phys. Reports **58** (1980) 269.

[16] J. C. Collins, D. E. Soper, Nucl. Phys. **B193** (1981) 381; **B197** (1982) 446; [Erratum **B213** (1983) 545].

[17] J. C. Collins, D. E. Soper and G. Sterman, Nucl. Phys. **B250** (1985) 199.

[18] G. Altarelli, R. K. Ellis, M. Greco and G. Martinelli, Nucl. Phys. **B246** (1984) 12.

[19] C. Davies and W. J. Stirling, Nucl. Phys. **B244** (1984) 337; C. Davies, B. Webber and W. J. Stirling, Nucl. Phys. **B256** (1985) 413.

[20] G. A. Ladinsky and C. P. Yuan, Phys. Rev. **D50** (1994) R4239.

[21] J. C. Collins and D. E. Soper, Phys. Rev. **D16** (1977) 2219.

[22] E. Mirkes, Nucl. Phys. **B387** (1992) 3.

[23] E. Mirkes, private communication.

[24] J. C. Collins, Phys. Rev. Lett. **42** (1979) 291.

[25] R. L. Thews, Phys. Rev. Lett. **43** (1979) 987, 1968(E).

[26] M. Guanziroli *et al.*: NA10 Collaboration, Z. Phys. **C37** (1988) 545.

[27] P. Chiapetta and M. LeBellac, Z. Phys. **C32** (1986) 521.

[28] S. J. Brodsky, G. P. Lepage and P. B. Mackenzie, Phys. Rev. **D28** (1983) 228; P. M. Stevenson, Phys. Rev. **D23**, 70 (1981); G. Grunberg, Phys. Lett. **95B** (1980) 70.

[29] P. L. McGaughey *et al.,* Phys. Rev. **D50** (1994) 3038.

[30] D. Antreasyan *et al.,* Phys. Rev. Lett. **48** (1982) 302.

Table 1. Inclusive cross section for Drell-Yan pairs in p-p collision
$$M^3 \frac{\mathrm{d}\sigma}{\mathrm{d}y\mathrm{d}M} \ [\mathrm{nb\,GeV}^2]$$
$\sqrt{s} = 200$ GeV

M [GeV]	Born MRS D$-'$	Born+LO MRS D$-'$	K_{th} MRS D$-'$	Born MRS D0$'$	Born+LO MRS D0$'$	K_{th} MRS D0$'$
3.0	0.9694E+01	0.1338E+02	1.380	0.9230E+01	0.1288E+02	1.395
4.0	0.9523E+01	0.1274E+02	1.338	0.9457E+01	0.1262E+02	1.334
5.0	0.9304E+01	0.1222E+02	1.313	0.9441E+01	0.1232E+02	1.305
6.0	0.8946E+01	0.1163E+02	1.299	0.9182E+01	0.1185E+02	1.290
7.0	0.8525E+01	0.1100E+02	1.289	0.8791E+01	0.1124E+02	1.278
8.0	0.8091E+01	0.1037E+02	1.281	0.8347E+01	0.1055E+02	1.264
9.0	0.7703E+01	0.9836E+01	1.276	0.8007E+01	0.1011E+02	1.262
10.0	0.7304E+01	0.9297E+01	1.272	0.7621E+01	0.9604E+01	1.260
11.0	0.6920E+01	0.8793E+01	1.270	0.7227E+01	0.9100E+01	1.259
12.0	0.6551E+01	0.8310E+01	1.268	0.6835E+01	0.8576E+01	1.254
13.0	0.6196E+01	0.7861E+01	1.268	0.6504E+01	0.8172E+01	1.256
14.0	0.5854E+01	0.7439E+01	1.270	0.6167E+01	0.7761E+01	1.258
15.0	0.5530E+01	0.7028E+01	1.271	0.5835E+01	0.7350E+01	1.259
16.0	0.5222E+01	0.6643E+01	1.272	0.5511E+01	0.6942E+01	1.259
17.0	0.4924E+01	0.6274E+01	1.274	0.5224E+01	0.6597E+01	1.262
18.0	0.4641E+01	0.5924E+01	1.276	0.4943E+01	0.6256E+01	1.265
19.0	0.4373E+01	0.5584E+01	1.276	0.4668E+01	0.5922E+01	1.268
20.0	0.4120E+01	0.5273E+01	1.279	0.4402E+01	0.5594E+01	1.270

[31] D. Antreasyan *et al.*, Phys. Rev. Lett. **48**, 302, (1982).

[32] A. S. Ito *et al.*, Phys. Rev. **D23**, 604, (1981).

[33] J. S. Conway *et al.*: E615 Collaboration, Phys. Rev. **D39** (1989) 92.

[34] S. Falciano *et al.*: NA10 Collaboration, Z. Phys. **C31** (1986) 513.

[35] A. Brandenburg, O. Nachtmann, and E. Mirkes, Z. Phys. **C60** (1993) 697.

[36] K.J. Eskola, R. Vogt and X.-N. Wang, "Nuclear Overlap Function", in this volume.

Table 2. Inclusive cross section for Drell-Yan pairs in p-p collision

$$M^3 \frac{\mathrm{d}\sigma}{\mathrm{d}y\mathrm{d}M}\ [\mathrm{nb\,GeV}^2]$$

$$\sqrt{s} = 500\ \mathrm{GeV}$$

M [GeV]	Born MRS D$-'$	Born+LO MRS D$-'$	K_{th} MRS D$-'$	Born MRS D$0'$	Born+LO MRS D$0'$	K_{th} MRS D$0'$
3.0	0.1411E+02	0.1906E+02	1.350	0.1125E+02	0.1582E+02	1.405
4.0	0.1408E+02	0.1844E+02	1.309	0.1234E+02	0.1652E+02	1.338
5.0	0.1380E+02	0.1773E+02	1.284	0.1282E+02	0.1666E+02	1.299
6.0	0.1350E+02	0.1722E+02	1.276	0.1297E+02	0.1662E+02	1.281
7.0	0.1308E+02	0.1656E+02	1.265	0.1288E+02	0.1630E+02	1.265
8.0	0.1264E+02	0.1586E+02	1.254	0.1268E+02	0.1585E+02	1.250
9.0	0.1221E+02	0.1527E+02	1.250	0.1242E+02	0.1545E+02	1.244
10.0	0.1175E+02	0.1462E+02	1.243	0.1209E+02	0.1494E+02	1.235
11.0	0.1139E+02	0.1415E+02	1.242	0.1180E+02	0.1455E+02	1.233
12.0	0.1105E+02	0.1368E+02	1.238	0.1151E+02	0.1414E+02	1.228
13.0	0.1070E+02	0.1323E+02	1.236	0.1119E+02	0.1373E+02	1.226
14.0	0.1036E+02	0.1280E+02	1.235	0.1086E+02	0.1331E+02	1.225
15.0	0.1004E+02	0.1238E+02	1.233	0.1054E+02	0.1290E+02	1.223
16.0	0.9729E+01	0.1199E+02	1.232	0.1022E+02	0.1250E+02	1.222
17.0	0.9433E+01	0.1161E+02	1.231	0.9914E+01	0.1211E+02	1.221
18.0	0.9149E+01	0.1125E+02	1.229	0.9611E+01	0.1172E+02	1.218
19.0	0.8869E+01	0.1090E+02	1.228	0.9306E+01	0.1133E+02	1.218
20.0	0.8602E+01	0.1056E+02	1.227	0.9011E+01	0.1095E+02	1.215
25.0	0.7461E+01	0.9168E+01	1.228	0.7844E+01	0.9564E+01	1.219
30.0	0.6505E+01	0.8006E+01	1.230	0.6797E+01	0.8292E+01	1.220
35.0	0.5701E+01	0.7037E+01	1.234	0.5976E+01	0.7328E+01	1.226
40.0	0.5039E+01	0.6249E+01	1.240	0.5262E+01	0.6481E+01	1.231
45.0	0.4492E+01	0.5593E+01	1.245	0.4704E+01	0.5830E+01	1.239
50.0	0.4079E+01	0.5099E+01	1.250	0.4261E+01	0.5305E+01	1.245
55.0	0.3807E+01	0.4787E+01	1.257	0.3972E+01	0.4978E+01	1.253
60.0	0.3704E+01	0.4685E+01	1.264	0.3862E+01	0.4872E+01	1.261
65.0	0.3868E+01	0.4918E+01	1.271	0.4027E+01	0.5114E+01	1.269
70.0	0.4518E+01	0.5779E+01	1.279	0.4693E+01	0.5998E+01	1.278
75.0	0.6259E+01	0.8050E+01	1.286	0.6487E+01	0.8349E+01	1.286

Table 3. Inclusive cross section for Drell-Yan pairs in p-p collision

$$M^3 \frac{\mathrm{d}\sigma}{\mathrm{d}y\mathrm{d}M}\ [\mathrm{nb\,GeV}^2]$$

$$\sqrt{s} = 5500\ \mathrm{GeV}$$

M [GeV]	Born MRS D$-'$	Born+LO MRS D$-'$	$K_{\rm th}$ MRS D$-'$	Born MRS D0$'$	Born+LO MRS D0$'$	$K_{\rm th}$ MRS D0$'$
3.0	0.7467E+02	0.9717E+02	1.301	0.1681E+02	0.2441E+02	1.452
4.0	0.7381E+02	0.9077E+02	1.229	0.2192E+02	0.2989E+02	1.363
5.0	0.7200E+02	0.8650E+02	1.201	0.2586E+02	0.3361E+02	1.299
6.0	0.6993E+02	0.8427E+02	1.205	0.2885E+02	0.3693E+02	1.279
7.0	0.6757E+02	0.7984E+02	1.181	0.3102E+02	0.3868E+02	1.247
8.0	0.6522E+02	0.7636E+02	1.170	0.3269E+02	0.4002E+02	1.224
9.0	0.6305E+02	0.7415E+02	1.176	0.3402E+02	0.4150E+02	1.219
10.0	0.6074E+02	0.7109E+02	1.170	0.3488E+02	0.4216E+02	1.208
11.0	0.5866E+02	0.6842E+02	1.166	0.3558E+02	0.4273E+02	1.201
12.0	0.5695E+02	0.6677E+02	1.172	0.3604E+02	0.4329E+02	1.201
13.0	0.5529E+02	0.6442E+02	1.165	0.3634E+02	0.4328E+02	1.190
14.0	0.5364E+02	0.6262E+02	1.167	0.3646E+02	0.4339E+02	1.190
15.0	0.5211E+02	0.6055E+02	1.161	0.3653E+02	0.4316E+02	1.181
16.0	0.5070E+02	0.5904E+02	1.164	0.3655E+02	0.4316E+02	1.180
17.0	0.4939E+02	0.5733E+02	1.160	0.3654E+02	0.4294E+02	1.175
18.0	0.4816E+02	0.5575E+02	1.157	0.3648E+02	0.4269E+02	1.170
19.0	0.4691E+02	0.5421E+02	1.155	0.3631E+02	0.4236E+02	1.166
20.0	0.4575E+02	0.5285E+02	1.155	0.3613E+02	0.4209E+02	1.165

Table 4. Inclusive cross section for Drell-Yan pairs in p-p collision

$$M^3 \frac{\mathrm{d}\sigma}{\mathrm{d}y\mathrm{d}M} \ [\mathrm{nb\,GeV}^2]$$

$\sqrt{s} = 14000$ GeV

M [GeV]	Born MRS D$-'$	Born+LO MRS D$-'$	$K_{\rm th}$ MRS D$-'$	Born MRS D0$'$	Born+LO MRS D0$'$	$K_{\rm th}$ MRS D0$'$
3.0	0.1671E+03	0.2167E+03	1.297	0.1878E+02	0.2814E+02	1.497
4.0	0.1659E+03	0.2073E+03	1.250	0.2623E+02	0.3637E+02	1.386
5.0	0.1616E+03	0.1918E+03	1.187	0.3253E+02	0.4260E+02	1.309
6.0	0.1564E+03	0.1797E+03	1.148	0.3774E+02	0.4773E+02	1.264
7.0	0.1508E+03	0.1642E+03	1.088	0.4184E+02	0.4911E+02	1.173
8.0	0.1454E+03	0.1632E+03	1.122	0.4522E+02	0.5374E+02	1.188
9.0	0.1405E+03	0.1612E+03	1.147	0.4806E+02	0.5802E+02	1.207
10.0	0.1355E+03	0.1534E+03	1.132	0.5013E+02	0.5998E+02	1.196
11.0	0.1309E+03	0.1459E+03	1.114	0.5191E+02	0.5996E+02	1.155
12.0	0.1269E+03	0.1468E+03	1.156	0.5341E+02	0.6409E+02	1.200
13.0	0.1231E+03	0.1406E+03	1.142	0.5459E+02	0.6431E+02	1.178
14.0	0.1193E+03	0.1374E+03	1.151	0.5543E+02	0.6556E+02	1.182
15.0	0.1160E+03	0.1333E+03	1.149	0.5609E+02	0.6611E+02	1.178
16.0	0.1129E+03	0.1295E+03	1.147	0.5665E+02	0.6650E+02	1.173
17.0	0.1100E+03	0.1249E+03	1.136	0.5713E+02	0.6639E+02	1.162
18.0	0.1072E+03	0.1209E+03	1.127	0.5750E+02	0.6622E+02	1.151
19.0	0.1045E+03	0.1186E+03	1.134	0.5765E+02	0.6661E+02	1.155
20.0	0.1019E+03	0.1146E+03	1.125	0.5776E+02	0.6618E+02	1.145
25.0	0.9120E+02	0.1037E+03	1.137	0.5786E+02	0.6657E+02	1.150
30.0	0.8283E+02	0.9371E+02	1.131	0.5698E+02	0.6505E+02	1.141
35.0	0.7664E+02	0.8638E+02	1.127	0.5601E+02	0.6346E+02	1.133
40.0	0.7179E+02	0.8131E+02	1.132	0.5510E+02	0.6264E+02	1.136
45.0	0.6848E+02	0.7750E+02	1.131	0.5479E+02	0.6214E+02	1.134
50.0	0.6693E+02	0.7538E+02	1.126	0.5550E+02	0.6257E+02	1.127
55.0	0.6752E+02	0.7622E+02	1.128	0.5774E+02	0.6518E+02	1.128
60.0	0.7175E+02	0.8103E+02	1.129	0.6286E+02	0.7095E+02	1.128
65.0	0.8248E+02	0.9345E+02	1.133	0.7378E+02	0.8349E+02	1.131
70.0	0.1068E+03	0.1207E+03	1.131	0.9728E+02	0.1098E+03	1.128
75.0	0.1648E+03	0.1864E+03	1.131	0.1526E+03	0.1722E+03	1.128
80.0	0.3334E+03	0.3776E+03	1.132	0.3136E+03	0.3541E+03	1.129

Table 5. Angular distribution factors for Drell-Yan pairs in p-p collision $\sqrt{s} = 200$ GeV, $M = 4$ GeV						
p_T [GeV]	$d\sigma/dM^2 dp_T{}^2 dy$ [GeV^{-6}] y = 0	A_0	A_1	$d\sigma/dM^2 dp_T{}^2 dy$ [GeV^{-6}] y = 3	A_0	A_1
0.2	0.367D-06	0.0072	0.0000	0.170D-06	0.0062	0.0140
0.4	0.772D-07	0.0296	0.0000	0.297D-07	0.0268	0.0385
0.6	0.302D-07	0.0653	0.0000	0.995D-08	0.0607	0.0708
0.8	0.153D-07	0.1108	0.0000	0.435D-08	0.1038	0.1082
1.0	0.888D-08	0.1623	0.0000	0.219D-08	0.1521	0.1477
1.2	0.563D-08	0.2166	0.0000	0.121D-08	0.2017	0.1871
1.4	0.380D-08	0.2713	0.0000	0.710D-09	0.2502	0.2245
1.6	0.267D-08	0.3247	0.0000	0.434D-09	0.2960	0.2590
1.8	0.194D-08	0.3757	0.0000	0.273D-09	0.3384	0.2900
2.0	0.144D-08	0.4236	0.0000	0.175D-09	0.3770	0.3173
2.2	0.110D-08	0.4683	0.0000	0.114D-09	0.4121	0.3410
2.4	0.846D-09	0.5095	0.0000	0.751D-10	0.4438	0.3613
2.6	0.663D-09	0.5473	0.0000	0.498D-10	0.4726	0.3786
2.8	0.525D-09	0.5820	0.0000	0.333D-10	0.4987	0.3930
3.0	0.420D-09	0.6136	0.0000	0.223D-10	0.5225	0.4050
3.2	0.339D-09	0.6425	0.0000	0.149D-10	0.5444	0.4148
3.4	0.276D-09	0.6688	0.0000	0.100D-10	0.5644	0.4227
3.6	0.226D-09	0.6928	0.0000	0.671D-11	0.5830	0.4289
3.8	0.187D-09	0.7148	0.0000	0.448D-11	0.6002	0.4337
4.0	0.155D-09	0.7347	0.0000	0.299D-11	0.6162	0.4372
4.2	0.129D-09	0.7530	0.0000	0.198D-11	0.6311	0.4397
4.4	0.108D-09	0.7696	0.0000	0.131D-11	0.6452	0.4412
4.6	0.915D-10	0.7849	0.0000	0.860D-12	0.6584	0.4418
4.8	0.775D-10	0.7988	0.0000	0.560D-12	0.6708	0.4418
5.0	0.659D-10	0.8117	0.0000	0.362D-12	0.6826	0.4411
5.2	0.563D-10	0.8235	0.0000	0.231D-12	0.6938	0.4399
5.4	0.483D-10	0.8343	0.0000	0.146D-12	0.7044	0.4382
5.6	0.416D-10	0.8442	0.0000	0.910D-13	0.7145	0.4361
5.8	0.359D-10	0.8534	0.0000	0.558D-13	0.7241	0.4337
6.0	0.312D-10	0.8618	0.0000	0.336D-13	0.7333	0.4309
6.2	0.271D-10	0.8696	0.0000	0.198D-13	0.7421	0.4279
6.4	0.236D-10	0.8768	0.0000	0.114D-13	0.7505	0.4246
6.6	0.207D-10	0.8836	0.0000	0.641D-14	0.7585	0.4212
6.8	0.181D-10	0.8898	0.0000	0.348D-14	0.7662	0.4177
7.0	0.159D-10	0.8955	0.0000	0.181D-14	0.7736	0.4139
7.2	0.141D-10	0.9009	0.0000	0.896D-15	0.7808	0.4099
7.4	0.124D-10	0.9058	0.0000	0.416D-15	0.7879	0.4058
7.6	0.110D-10	0.9105	0.0000	0.180D-15	0.7948	0.4014
7.8	0.977D-11	0.9149	0.0000	0.722D-16	0.8013	0.3970
8.0	0.869D-11	0.9189	0.0000	0.268D-16	0.8073	0.3929

Table 6. Angular distribution factors for Drell-Yan pairs in p-p collision $\sqrt{s} = 5500$ GeV, $M = 4$ GeV						
p_T [GeV]	$d\sigma/dM^2dp_T{}^2dy$ [GeV^{-6}] y = 0	A_0	A_1	$d\sigma/dM^2dp_T{}^2dy$ [GeV^{-6}] y = 3	A_0	A_1
0.2	0.389D-05	0.0085	0.0000	0.545D-05	0.0081	-0.0071
0.4	0.844D-06	0.0341	0.0000	0.118D-05	0.0329	-0.0154
0.6	0.337D-06	0.0736	0.0000	0.471D-06	0.0714	-0.0238
0.8	0.173D-06	0.1226	0.0000	0.241D-06	0.1194	-0.0317
1.0	0.101D-06	0.1768	0.0000	0.141D-06	0.1730	-0.0387
1.2	0.647D-07	0.2328	0.0000	0.905D-07	0.2287	-0.0448
1.4	0.438D-07	0.2882	0.0000	0.614D-07	0.2841	-0.0498
1.6	0.309D-07	0.3415	0.0000	0.434D-07	0.3377	-0.0538
1.8	0.225D-07	0.3916	0.0000	0.317D-07	0.3883	-0.0569
2.0	0.168D-07	0.4383	0.0000	0.237D-07	0.4357	-0.0592
2.2	0.128D-07	0.4813	0.0000	0.180D-07	0.4795	-0.0607
2.4	0.990D-08	0.5207	0.0000	0.140D-07	0.5198	-0.0615
2.6	0.776D-08	0.5566	0.0000	0.110D-07	0.5567	-0.0618
2.8	0.615D-08	0.5895	0.0000	0.872D-08	0.5903	-0.0616
3.0	0.493D-08	0.6193	0.0000	0.700D-08	0.6210	-0.0611
3.2	0.398D-08	0.6464	0.0000	0.567D-08	0.6489	-0.0602
3.4	0.325D-08	0.6712	0.0000	0.463D-08	0.6743	-0.0591
3.6	0.267D-08	0.6936	0.0000	0.381D-08	0.6975	-0.0577
3.8	0.220D-08	0.7142	0.0000	0.315D-08	0.7186	-0.0562
4.0	0.183D-08	0.7329	0.0000	0.262D-08	0.7378	-0.0546
4.2	0.153D-08	0.7500	0.0000	0.220D-08	0.7554	-0.0529
4.4	0.129D-08	0.7657	0.0000	0.185D-08	0.7714	-0.0512
4.6	0.109D-08	0.7801	0.0000	0.157D-08	0.7861	-0.0494
4.8	0.928D-09	0.7932	0.0000	0.133D-08	0.7996	-0.0476
5.0	0.793D-09	0.8054	0.0000	0.114D-08	0.8120	-0.0457
5.2	0.680D-09	0.8166	0.0000	0.977D-09	0.8234	-0.0439
5.4	0.586D-09	0.8268	0.0000	0.841D-09	0.8338	-0.0421
5.6	0.506D-09	0.8363	0.0000	0.727D-09	0.8434	-0.0403
5.8	0.439D-09	0.8450	0.0000	0.631D-09	0.8523	-0.0385
6.0	0.383D-09	0.8532	0.0000	0.550D-09	0.8605	-0.0368
6.2	0.335D-09	0.8608	0.0000	0.480D-09	0.8681	-0.0351
6.4	0.293D-09	0.8677	0.0000	0.421D-09	0.8752	-0.0334
6.6	0.258D-09	0.8743	0.0000	0.370D-09	0.8817	-0.0318
6.8	0.228D-09	0.8803	0.0000	0.326D-09	0.8878	-0.0302
7.0	0.202D-09	0.8860	0.0000	0.288D-09	0.8934	-0.0286
7.2	0.179D-09	0.8913	0.0000	0.256D-09	0.8987	-0.0271
7.4	0.159D-09	0.8962	0.0000	0.227D-09	0.9036	-0.0256
7.6	0.142D-09	0.9008	0.0000	0.203D-09	0.9082	-0.0242
7.8	0.127D-09	0.9052	0.0000	0.181D-09	0.9124	-0.0228
8.0	0.114D-09	0.9092	0.0000	0.162D-09	0.9165	-0.0214